Chapter 8
Transient Chaos in Higher Dimensions

This chapter is devoted to transient chaos in higher-dimensional dynamical systems. The defining characteristic of high-dimensional transient chaos is that the underlying chaotic set has unstable dimension more than one, in contrast to most situations discussed in previous chapters, where chaotic sets have one unstable dimension. We shall call nonattracting chaotic sets with one unstable dimension *low-dimensional*, while those having unstable dimension greater than one *high-dimensional*. The increase in the unstable dimension from one represents a highly nontrivial extension in terms of what has been discussed so far about transient chaos. For instance, the PIM-triple algorithm, which is effective for finding an approximate continuous trajectory on a low-dimensional chaotic saddle, is generally not applicable to high-dimensional chaotic saddles. In a scattering experiment in high-dimensional phase space, the presence of a chaotic saddle cannot guarantee that chaos can be physically observed. In particular, if the box-counting dimension of the chaotic saddle is low, its stable manifold may not intersect a set of initial conditions prepared in the corresponding physical space; only when the dimension is high enough can chaotic scattering be observed.

First we present a prototypical example, the three-dimensional baker map, for which a basic property of high-dimensional hyperbolic systems can be seen explicitly: different numbers of the expanding and the contracting dimensions. Next we show how the escape rate and the metric entropy can be expressed in terms of the Lyapunov exponents in high-dimensional maps, present derivations for the dimension formulas of the stable and the unstable manifolds for high-dimensional chaotic saddles, and address their applicability and the concept of typicality using particular examples. An efficient algorithm, the stagger-and-step method, is then described for computing high-dimensional chaotic saddles. Chaotic scattering in three-degree-of-freedom systems is presented, the conditions for the observability of chaotic scattering are formulated, and new features of the scattering dynamics are discussed. The phenomenon of superpersistent chaotic transients and applications are also treated in this chapter.

Y.-C. Lai and T. Tél, *Transient Chaos: Complex Dynamics on Finite-Time Scales*,
Applied Mathematical Sciences 173, DOI 10.1007/978-1-4419-6987-3_8,

8.1 Three-Dimensional Open Baker Map

Three-dimensional invertible maps arise on stroboscopic or Poincaré sections of four-dimensional flows. There are two classes of hyperbolic maps: (1) maps with one unstable and two stable directions (type I) and (2) maps with two unstable and one stable direction (type II). The escape dynamics in these two cases are generally different.

The open three-dimensional baker map is the spatial extension [165] of the planar baker map treated in Sect. 2.5. Because of the odd dimensionality of the map, the number of unstable directions is different from that of stable directions. Consequently, such maps, even if they preserve volume, cannot describe Hamiltonian systems. Nonetheless, in the volume-preserving case they can be used to model the advection by three-dimensional time-periodic flows (see [165] and Chap. 10). The map, denoted by M, is defined on the unit cube, and its action is shown in Fig. 8.1a.

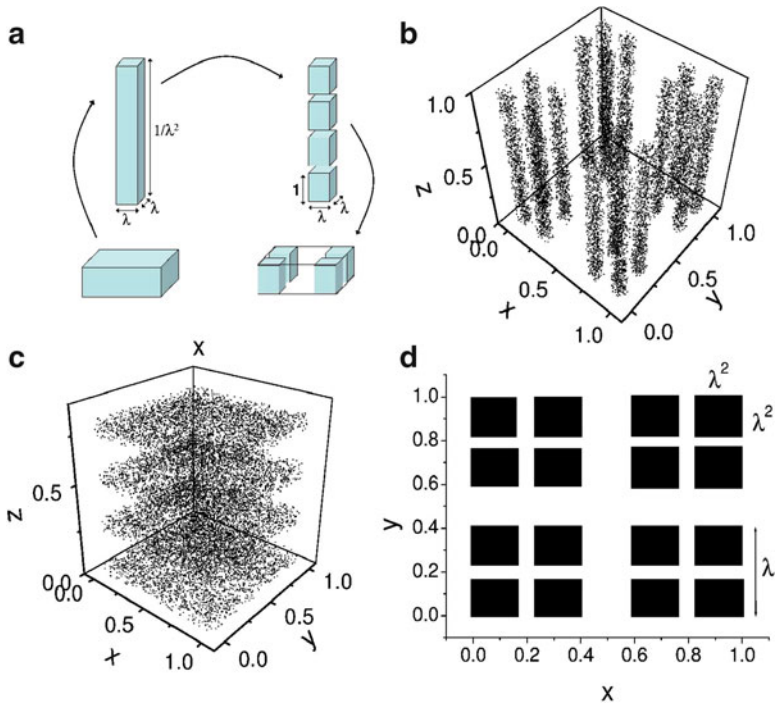

Fig. 8.1 (**a**) Illustration of the action of one iteration of the three-dimensional open baker map M on the unit cube (the restraining region Γ) for type-I dynamics. For simplicity the parameters are chosen to be $b = c \equiv \lambda$ and $a = 1/\lambda^2$ (volume-preserving case). Note that the drawing is not to scale. (**b**) For $\lambda = 0.35$, surviving points after two iterations of the map with initial conditions chosen randomly from the cube. (**c**) The same as (**b**), but for the inverse map M^{-1} (type-II dynamics). (**d**) For $\lambda = 0.35$, intersection with a horizontal plane of the set of surviving points after two iterations of the map [771] (with kind permission from Elsevier Science)

One iteration of the map consists of two actions. Firstly, the x and y directions are contracted by factors b and c, respectively, where $b, c < 1/2$, while the z direction undergoes an expansion by a factor $a > 4$. Under the transformation, the cube turns into a long, thin rectangular slab with its long edge along the z-axis, as shown in Fig. 8.1a. Secondly, four pieces of unit height of this slab are selected and placed in the four corners of the cube. The pieces of the slab that are not selected are discarded and are regarded as having escaped (Fig. 8.1a). The map has two contracting directions and one expanding direction, and is therefore of type I. For the inverse map M^{-1}, stable directions turn into unstable ones, and vice versa. As a result, M^{-1} has one stable and two unstable directions, and is of type II. The two generic types of three-dimensional hyperbolic maps can thus be conveniently studied using the baker map. Since hyperbolic systems are structurally stable, generality is not lost by assuming any particular form for M.

Because the contracting and the expanding directions of M (and also M^{-1}) are aligned with the x-, y-, and z-axes, it is not difficult to visualize the stable and the unstable manifolds: the stable manifold of M is a Cantor set of planes parallel to the horizontal (x, y)-plane, and the unstable manifold is a Cantor set of vertical segments. We can visualize these manifolds by iterating M forward a given number of times for many initial conditions chosen randomly within the unit cube. The distribution of points that have not escaped approximate the unstable manifold of M, which is the stable manifold of M^{-1}. Conversely, iterating backward (or iterating M^{-1} forward) in time gives the stable manifold of M (or the unstable manifold of M^{-1}). These results are shown in Fig. 8.1b, c.

Consider now the unstable manifold of M, as shown in Fig. 8.1b. Since it is made up of vertical line segments, and since the expansion and the contraction rates are uniform, we can restrict attention to the intersection of the unstable manifold with a horizontal plane. This is depicted in Fig. 8.1d, where the intersection of the set of surviving points after two iterations of M with a horizontal plane is shown. In the limit of an infinite number of iterations, a double Cantor set in the plane is formed with partial box-counting dimensions $D_0^{(2)} = \ln 2/\ln(1/b)$ and $D_0^{(3)} = \ln 2/\ln(1/c)$ along the stable manifolds. The unstable manifold is the product of this Cantor set and a one-dimensional line segment; its dimension is

$$D_{\mathrm{u},0} = 1 + \ln 2 \left(\frac{1}{\ln(1/b)} + \frac{1}{\ln(1/c)} \right). \tag{8.1}$$

Similar reasoning can be applied to the stable manifold. The partial box-counting dimension along the unstable direction is set by the stretching factor a. Since in each step a factor $1/a$ of the slab remains in the unit cube, we have $D_0^{(1)} = \ln 4/\ln a$. The stable manifold is the product of this Cantor set with a plane. We obtain

$$D_{\mathrm{s},0} = 2 + \frac{\ln 4}{\ln a}. \tag{8.2}$$

The manifold dimensions satisfy

$$1 < D_{\mathrm{u},0} < 3, \quad 2 < D_{\mathrm{s},0} < 3. \tag{8.3}$$

The chaotic saddle is the intersection of the stable and the unstable manifolds, and its box-counting dimension is

$$D_0 = \sum_{j=1}^{3} D_0^{(j)} = D_{\mathrm{u},0} + D_{\mathrm{s},0} - 3. \tag{8.4}$$

The baker map has one positive Lyapunov exponent $\lambda_1^+ = \ln a$ and two negative ones of magnitudes $\lambda_1^- = \ln(1/b)$ and $\lambda_2^- = \ln(1/c)$. The escape rate is $\kappa = \ln(a/4)$, and the topological entropy is $K_0 = \ln 4$.

The inverted map has two positive Lyapunov exponents, $\lambda_1^+ = \ln(1/b)$ and $\lambda_2^+ = \ln(1/c)$, and a negative exponent of magnitude $\lambda_1^- = \ln a$. The topology of the escaping process in the inverted map is different from that of M, which is also reflected by the difference in the values of the escape rate (for the inverted map it is $\kappa = -\ln(4bc)$). The manifold dimensions can be obtained from (8.1) and (8.2) by interchanging the indices u and s.

In general, the structures of the stable and the unstable manifolds for the two types of generic maps are topologically similar to those shown in Fig. 8.1. In particular, for type-I maps, the stable manifold is a Cantor set of surfaces, and the unstable manifold is a Cantor set of one-dimensional curves (vice versa for type-II maps). Also, the inequalities (8.3) hold in general for type-I maps.

Based on (8.3), we observe that for type-II maps, the dimension $D_{\mathrm{s},0}$ of the stable manifold may be less than 2. In this case, the stable manifold has generically a null intersection with a one-dimensional curve (see (8.52)), and thus the lifetime distribution along a line is a smooth function, even though there is a fractal invariant set. For $D_{\mathrm{s},0} > 2$, however, a typical lifetime function has a fractal set of singularities that is similar to that in Fig. 1.5. The transition point defined by $D_{\mathrm{s},0} = 2$ is given for the map M^{-1} by the condition $1/\ln b + 1/\ln c = -1/\ln 2$. If the map is of type I, however, this transition does not occur. This is a nontrivial difference between the dynamics of the two types of map. We will consider a similar problem in the context of high-dimensional chaotic scattering in Sect. 8.5.1.

8.2 Escape Rate, Entropies, and Fractal Dimensions for Nonattracting Chaotic Sets in Higher Dimensions

8.2.1 Escape Rate and Entropies

Consider an open dynamical system described by an N-dimensional map. For a general chaotic saddle in the N-dimensional phase space, there are U positive and

S negative average Lyapunov exponents, where $U + S = N$. The exponents can be ordered as follows

$$\lambda_U^+ \geq \lambda_{U-1}^+ \geq \cdots \geq \lambda_1^+ > 0 \geq -\lambda_1^- \geq \cdots \geq -\lambda_{S-1}^- \geq -\lambda_S^-. \tag{8.5}$$

Thus all quantities $\lambda_j^{+,-}$ are positive, and smaller values of the subscripts j correspond to Lyapunov exponents that are closer to zero in magnitude. Analogous to the low-dimensional cases, one can define partial box-counting and information dimensions $D_0^{(j)}$ and $D_1^{(j)}$, respectively, for any direction j along which an average Lyapunov exponent exists. The total dimension D_i ($i = 0, 1$) of the nonattracting set is the sum of the partial dimensions:

$$D_i = \sum_j D_i^{(j)}, \quad i = 0, 1. \tag{8.6}$$

General expressions for the escape rate and the metric entropy follow from the extension of the information-theoretic arguments in Sect. 2.6.3 for two-dimensional maps [380].

Along the stable directions particles cannot escape. Along an unstable direction, they cannot escape either if the partial information dimension is $D_1^{(j)} = 1$ (more precisely, the escape is slower than exponential). Exponential escape is possible only along unstable directions for which $D_1^{(j)} < 1$. Since escapes in different directions j are independent of each other, and the mean velocity of the information flow is λ_j^+, the escape rate is the sum of contributions from all unstable directions:

$$\kappa = \sum_{j=1}^{U} \lambda_j^+ (1 - D_1^{(j)}). \tag{8.7}$$

The metric entropy, as discussed in Sect. 2.6.3, is the rate at which information stored in the insignificant digits of the initial condition flows toward the significant ones. This flow occurs along the unstable directions only. Since the information dimension and the Lyapunov exponent characterize the density of information and the mean velocity of the flow, respectively, we have

$$K_1 = \sum_{j=1}^{U} \lambda_j^+ D_1^{(j)}. \tag{8.8}$$

Using (8.7), one can write K_1 as

$$K_1 = \sum_{j=1}^{U} \lambda_j^+ - \kappa. \tag{8.9}$$

This relation implies that the degree of unpredictability of the dynamics on the nonattracting set, measured by K_1, is only a fraction of the total flux $\sum_{j=1}^{U} \lambda_j^+$ of digits, because of the loss of information due to escape. Formula (8.9) is an extension

of Pesin's relation [564], according to which the metric entropy is the sum of all positive Lyapunov exponents for closed N-dimensional maps.

In invertible systems, the same amount of information flows in along the stable directions as the amount flowing out along the unstable directions, i.e.,

$$\sum_{j=1}^{S} \lambda_j^- D_1^{(j)} = \sum_{j=1}^{U} \lambda_j^+ D_1^{(j)}. \tag{8.10}$$

A special case of this rule has been observed in (2.80) for two-dimensional maps.

The relations (8.7), (8.8), and (8.9) are valid for noninvertible and nonhyperbolic cases as well. For example, two-dimensional maps with two positive Lyapunov exponents are covered by these formulas, such as the repellers of the complex quadratic map, the Julia sets shown in Fig. 1.3b, which are topologically a circle. Due to the symmetry, both Lyapunov exponents and both partial information dimensions are equal. Equations (8.7) and (8.8) then imply, with the notation $\lambda_1^+ = \lambda_2^+ \equiv \lambda$, that

$$\kappa = \lambda(2 - D_1), \quad K_1 = \lambda D_1. \tag{8.11}$$

Since the natural measure of the connected Julia set is known to have information dimension $D_1 = 1$ [84], we have $\kappa = \lambda = K_1$. This is to be contrasted with the properties of isolated repeller points of the complex quadratic maps for which $D_1 = 0$ and hence, $\kappa = 2\lambda$ with $K_1 = 0$.

Obtaining an expression for the topological entropy is more complicated. As generalizations of (2.22) and (2.81), we have [380]

$$K_0 = \sum_{j=1}^{U} \lambda_j^+ - \kappa + \frac{1}{2} \sum_{j,k}^{U} Q_{2,j,k}^+ + \cdots \tag{8.12}$$

and

$$\kappa = \sum_{j=1}^{U} \lambda_j^+ (1 - D_0^{(j)}) + \frac{1}{2} \sum_{j,k}^{U} (1 - D_0^{(j)})(1 - D_0^{(k)}) Q_{2,j,k}^+ + \cdots, \tag{8.13}$$

where $Q_{2,j,k}^+$ represents the cumulant of the Lyapunov exponents from expanding directions j and k [380].

8.2.2 Dimension Formulas for High-Dimensional Chaotic Saddles

For high-dimensional chaotic saddles, dimension formulas for the entire stable and unstable manifolds can be derived. Our treatment here follows that of Hunt et al. [347]. Imagine normalizing the size of the chaotic saddle so that it can be enclosed

by a cube of unit length. This cube is considered the restraining region. For a hyperbolic saddle, the cube can be regarded as having edges parallel to directions of stretching and contraction as defined by the Lyapunov exponents λ_j^+ and $-\lambda_i^-$. Now uniformly sprinkle a large number of points in the cube and iterate them forward n times. The resulting trajectory points will be distributed to slabs within the cube of dimensions

$$1 \times 1 \times \cdots \times 1 \times \mathrm{e}^{-\lambda_1^- n} \times \mathrm{e}^{-\lambda_2^- n} \times \cdots \times \mathrm{e}^{-\lambda_S^- n}, \tag{8.14}$$

where there are U slab edges of unit length in the U unstable directions. Let $N^{(\mathrm{sl})}(n)$ be the number of slabs at time n. Since trajectory points within these slabs remain in the cube for at least n iterates, the total content of the slabs is proportional to $\exp(-\kappa n)$, where κ is the escape rate from the chaotic saddle. Since the density of points has increased by a factor of $\exp\left[\left(\sum_{j=1}^{S} \lambda_j^- - \sum_{j=1}^{U} \lambda_j^+\right) n\right]$, we have

$$N^{(\mathrm{sl})}(n)\mathrm{e}^{-\lambda_U^+ n} \times \mathrm{e}^{-\lambda_{U-1}^+ n} \times \cdots \times \mathrm{e}^{-\lambda_1^+ n} = N^{(\mathrm{sl})}(n) \exp\left(-\sum_{j=1}^{U} \lambda_j^+ n\right) \sim \exp(-\kappa n). \tag{8.15}$$

Using (8.9), we see that (8.15) implies

$$N^{(\mathrm{sl})}(n) \sim \mathrm{e}^{K_1 n}. \tag{8.16}$$

Since at time n, trajectory points that have not left the restraining region are distributed in the vicinity of the unstable manifold, we need to examine the set of $N^{(\mathrm{sl})}(n)$ in (8.14). Say we wish to cover them using small N-dimensional cubes. A natural choice for the edge length of such a cube is that set by the contraction of the dynamics. Since there are several contracting directions, we have different choices. Take

$$\varepsilon_i = \exp(-\lambda_{i+1}^- n) \tag{8.17}$$

with index i between 0 and $S-1$. The required number of cubes is then

$$\begin{aligned} N^{(u)}(\varepsilon_i) &= \left(\frac{1}{\varepsilon_i}\right)^U \left(\frac{\mathrm{e}^{-\lambda_1^- n}}{\varepsilon_i}\right)\left(\frac{\mathrm{e}^{-\lambda_2^- n}}{\varepsilon_i}\right)\cdots\left(\frac{\mathrm{e}^{-\lambda_i^- n}}{\varepsilon_i}\right) N^{(\mathrm{sl})}(n) \\ &\sim \left(\frac{1}{\varepsilon_i}\right)^{U+i} \exp[-(\lambda_1^- + \lambda_2^- + \cdots + \lambda_i^-)n + K_1 n], \end{aligned} \tag{8.18}$$

where (8.16) has been used.

The information dimension of any invariant measure can be considered as the box-counting dimension of regions containing most of the measure, i.e., regions covering typical sets taken with respect to the measure (see, e.g., [773]). Applying

this to the c-measure of the unstable manifold, represented by the slabs at time n, we find an approximation to the information dimension of the unstable manifold for large n:

$$D_{\mathrm{u},1}(i) = \frac{\ln N^{(u)}(\varepsilon_i)}{\ln(1/\varepsilon_i)} = U + i + \frac{K_1 - (\lambda_1^- + \lambda_2^- + \cdots + \lambda_i^-)}{\lambda_{i+1}^-}. \tag{8.19}$$

The covering by the set of ε_i-cubes may not be optimal, so $D_{\mathrm{u},1}(i)$ is an upper bound of $D_{\mathrm{u},1}$: $D_{\mathrm{u},1} \le D_{\mathrm{u},1}(i)$. It is thus necessary to minimize $D_{\mathrm{u},1}(i)$ over i to obtain the true dimension. A convenient way to find the minimum of $D_u(i)$ is to examine the quantity $D_{\mathrm{u},1}(i+1) - D_{\mathrm{u},1}(i)$, which is

$$D_{\mathrm{u},1}(i+1) - D_{\mathrm{u},1}(i) = \left(\frac{1}{\lambda_{i+1}^-} - \frac{1}{\lambda_{i+2}^-}\right) \times [(\lambda_1^- + \lambda_2^- + \cdots + \lambda_i^- + \lambda_{i+1}^-) - K_1].$$

Since $\lambda_{i+1}^- \le \lambda_{i+2}^-$, we see that $D_{\mathrm{u},1}(i+1) - D_{\mathrm{u},1}(i)$ is positive (negative) if the term in the square brackets is positive (negative). Thus, if there exists a value I of i such that

$$\lambda_1^- + \lambda_2^- + \cdots + \lambda_I^- + \lambda_{I+1}^- \ge K_1 \ge \lambda_1^- + \lambda_2^- + \cdots + \lambda_I^-, \tag{8.20}$$

then $D_{\mathrm{u},1}(I+1) - D_{\mathrm{u},1}(I)$ is positive or zero but $D_{\mathrm{u},1}(I) - D_{\mathrm{u},1}(I-1)$ is negative or zero. That is, we have $D_{\mathrm{u},1}(I) \le D_{\mathrm{u},1}(I+1)$ and $D_{\mathrm{u},1}(I) \le D_{\mathrm{u},1}(I-1)$ simultaneously, indicating that the value of I chosen in (8.20) is the optimal choice of the index i that yields the true dimension $D_{\mathrm{u},1}$:

$$D_{\mathrm{u},1} = U + I + \frac{K_1 - (\lambda_1^- + \lambda_2^- + \cdots + \lambda_I^-)}{\lambda_{I+1}^-}, \tag{8.21}$$

where I is the largest index for which the numerator of (8.21) is still positive.

The information dimension of the natural measure of the stable manifold can be obtained in a similar manner. To see where the slabs of size (8.14) (whose number is $N^{(\mathrm{sl})}(n)$) come from within the cube, we iterate them backward n times and obtain $N^{(\mathrm{sl})}(n)$ slabs of initial conditions, each of dimension

$$\mathrm{e}^{-\lambda_U^+ n} \times \mathrm{e}^{-\lambda_{U-1}^+ n} \times \cdots \times \mathrm{e}^{-\lambda_1^+ n} \times 1 \times \cdots \times 1, \tag{8.22}$$

where for each slab there are S edges of unit length. Since initial conditions leading to trajectories that remain in the restraining region for at least n iterates are found in the slabs of size given by (8.22), we can cover them by small cubes of properly chosen edge length $\varepsilon_j = \exp(-\lambda_{j+1}^+ n)$ and obtain an upper bound $D_{\mathrm{s},1}(j)$ for the true dimension $D_{\mathrm{s},1}$. Reasoning similar to that in the derivation of $D_{\mathrm{u},1}$ yields the following optimal choice of the index J:

$$\lambda_1^+ + \lambda_2^+ + \cdots + \lambda_J^+ + \lambda_{J+1}^+ \geq K_1 \geq \lambda_1^+ + \lambda_2^+ + \cdots + \lambda_J^+, \tag{8.23}$$

which gives

$$D_{\mathrm{s},1} = S + J + \frac{K_1 - (\lambda_1^+ + \lambda_2^+ + \cdots + \lambda_J^+)}{\lambda_{J+1}^+}, \tag{8.24}$$

where J is the largest index for which the numerator of (8.24) is still positive.

The information dimension of the chaotic saddle, which is the intersection of its stable and unstable manifolds, is

$$D_1 = D_{\mathrm{u},1} + D_{\mathrm{s},1} - N = (I + J) + \frac{K_1 - \sum_{i=1}^{I} \lambda_i^-}{\lambda_{I+1}^-} + \frac{K_1 - \sum_{j=1}^{J} \lambda_j^+}{\lambda_{J+1}^+}. \tag{8.25}$$

This is a generalization of (8.4) for the information dimension of the invariant set to any N-dimensional map.

In the case of a chaotic attractor, we have $\kappa = 0$, so K_1 is the sum of all positive Lyapunov exponents. This leads to the information dimension D_1 of the attractor, since $D_1 = D_{\mathrm{u},1}$ with (8.21), which is the Kaplan–Yorke formula in higher dimensions [564]. Note that the index I in $D_{\mathrm{u},1}$ is then such that $(\sum_{j=1}^{U} \lambda_j^+ - \sum_{i=1}^{I} \lambda_i^-)$ is positive but $(\sum_{j=1}^{U} \lambda_j^+ - \sum_{i=1}^{I+1} \lambda_i^-)$ is negative. Furthermore, from (8.23) we see that $J = U - 1$ and thus $D_{\mathrm{s},1} = S + U = N$, i.e., the stable manifold is space-filling, as it should for a basin of attraction.

A special case is high-dimensional maps derived from Hamiltonian flows. Due to the symplectic structure of the dynamics, positive and negative Lyapunov exponents arise in pairs: $\lambda_j^+ = \lambda_j^-$. The manifold dimensions in Hamiltonian systems therefore coincide:

$$D_{\mathrm{u},1} = D_{\mathrm{s},1} = (D_1 + N)/2. \tag{8.26}$$

For a chaotic saddle of a two-dimensional map with one positive Lyapunov exponent $\lambda_1 \equiv \lambda_1^+ > 0$ and one negative exponent $\lambda_2 \equiv -\lambda_1^- < 0$, we have $U = 1$ and $S = 1$. In dissipative or area-preserving systems, we have $\lambda_1 + \lambda_2 \leq 0$. As a result, $\lambda_1 + \lambda_2 - \kappa < 0$. Thus $K_1 \leq |\lambda_2|$, and we have $I = 0$ and $J = 0$, which leads to the corresponding formulas derived in Sect. 2.6.2.

Readers should keep in mind that the dimension formulas (8.21), (8.24), and (8.25) are derived heuristically under the assumption that the chaotic saddle is hyperbolic. While there is numerical evidence for a class of open systems (see, e.g., [745, 746]) with nonhyperbolic high-dimensional chaotic saddles, there has been no systematic numerical study to validate these formulas, although they are conjectured to apply to *typical* systems [347]. This can be seen heuristically by noting that for such a system, small perturbations cannot change its properties and dynamical invariants. Atypical systems, on the other hand, are those whose dynamical invariants change under small perturbations. In the next section we will consider specific examples to contrast typical versus atypical systems with respect to their dimensions.

8.3 Models Testing Dimension Formulas

Because of the heuristic nature in the derivation of the dimension formulas, it is insightful to examine representative models for which the quantities involved in the formulas can be obtained analytically or numerically. The following two models, due to Sweet and Ott [746], will be used: (1) an analytic two-dimensional, noninvertible expanding map, and (2) a three-dimensional billiard scatterer.

8.3.1 Two-Dimensional Noninvertible Map Model

8.3.1.1 Natural Measure and Lyapunov Exponents

The map is of the form

$$\begin{aligned} x_{n+1} &= 2x_n \bmod(1), \\ y_{n+1} &= \alpha(x_n)y_n + \frac{\eta}{2\pi}\sin(2\pi x_n), \end{aligned} \tag{8.27}$$

where $\alpha(x) > 1$ and the map is defined in the region $-\infty \le y \le +\infty$ and $0 \le x \le 1$. The variable x can be considered as an angle-like variable, so the map is defined on a cylinder. The following piecewise constant function was chosen for $\alpha(x)$:

$$\alpha(x) = \begin{cases} \alpha_1, & 0 < x < 1/2, \\ \alpha_2, & 1/2 < x < 1, \end{cases} \tag{8.28}$$

where $1 < \alpha_1 \le \alpha_2$. Because $\alpha(x) > 1$, almost all initial conditions go either to $y = +\infty$ or to $y = -\infty$, which can be regarded as two attractors, and there is a boundary between the two basins of attraction near $y = 0$. The boundary is an invariant set, which is ergodic because of the chaotic dynamics in x. In fact, the invariant set is a chaotic repeller with two positive Lyapunov exponents. The Jacobian matrix of (8.27) is

$$J(x) = \begin{bmatrix} 2 & 0 \\ \eta\cos(2\pi x) & \alpha(x) \end{bmatrix}, \tag{8.29}$$

so the two Lyapunov exponents of the chaotic repeller are

$$\lambda_a = p\ln\alpha_1 + (1-p)\ln\alpha_2 \quad \text{and} \quad \lambda_b = \ln 2, \tag{8.30}$$

where p is the measure of the region $x < 1/2$. Note that for the one-dimensional map $x_{n+1} = 2x_n \bmod(1)$ alone, we have $p = 1/2$ because a random initial condition leads to a trajectory that visits the intervals $[0, 1/2]$ and $[1/2, 1]$ with equal probabilities. However, the presence of the y-dynamics changes the natural measure

of the x-intervals. To calculate p, consider the strip $-K \le y \le K$ on the cylinder and sprinkle a large number of initial conditions uniformly in the strip with density ρ_0. A vertical line segment of length $2K$ at $x = x_0$ and centered at $y_0 = 0$ iterates to $x = x_1$, and its center will be at $y_1 = (\eta/2\pi)\sin(2\pi x_0)$. This line segment will at the same time be stretched vertically by a factor of $\alpha(x_0)$. The endpoints of the segment will then be at $(\eta/2\pi)\sin(2\pi x_0) \pm \alpha(x_0)K$. In order for the segment to span the initial strip $-K \le y \le K$, it is necessary to choose K such that $(\eta/2\pi)\sin(2\pi x_0) - \alpha(x_0)K < -K$ (if $y_1 > 0$) or $(\eta/2\pi)\sin(2\pi x_0) + \alpha(x_0)K > K$ (if $y_1 < 0$). In either case, it is necessary to have

$$K > (\eta/2\pi)|\sin(2\pi x_0)|/[\alpha(x_0) - 1],$$

which can be satisfied if we choose

$$K > (\eta/2\pi)/(\alpha_1 - 1).$$

Since the map stretches a region uniformly in the x-direction by a factor of two and in the y-direction by a factor of either α_1 or α_2, after one iterate the density will still be uniform in the initial strip, and it is $\rho_1 = [(\alpha_1^{-1} + \alpha_2^{-1})/2]\rho_0$. After n iterations, the density in the strip becomes

$$\rho_n = \left[\frac{1}{2}(\alpha_1^{-1} + \alpha_2^{-1})\right]^n \rho_0,$$

which decays exponentially with time ($\rho_n = \rho_0 \exp(-\kappa n)$) with escape rate

$$\kappa = \ln \frac{2\alpha_1\alpha_2}{\alpha_1 + \alpha_2}. \tag{8.31}$$

Since both Lyapunov exponents are positive, the chaotic repeller formally coincides with its stable manifold. It suffices thus to calculate the natural measure of the stable manifold. To do so, note that in the x-direction, an interval of length 2^{-n} maps to the unit interval after n iterates. It is thus useful to divide the initial strip $-K \le y \le K$ into 2^n vertical substrips. In substrip i, we have $x \in s_i^{(n)} = [(i-1)/2^n, i/2^n]$ ($i = 1, \ldots, 2^n$). For a uniform distribution of $N_0 = 2K\rho_0$ points in the strip $-K \le y \le K$, $N_0/2^n$ will be in $s_i^{(n)}$ and we ask how many of those there are whose trajectories do not leave the strip at time n. Assume that in n iterates, the substrip $s_i^{(n)}$ experiences $n_1(i)$ and $n_2(i)$ vertical stretches by α_1 and α_2, respectively, where $n_1(i) + n_2(i) = n$. The initial subregion in $s_i^{(n)}$ that can survive at least n iterates has vertical height $2K\alpha_1^{-n_1(i)}\alpha_2^{-n_2(i)}$. There are then

$$\frac{2K\alpha_1^{-n_1(i)}\alpha_2^{-n_2(i)}}{2K} \cdot \frac{N_0}{2^n} = 2^{-n}\alpha_1^{-n_1(m)}\alpha_2^{-n_2(m)}N_0$$

such initial conditions. The measure of the stable manifold in $s_i^{(n)}$ is

$$\mu_i^{(n)} = \frac{2^{-n}\alpha_1^{-n_1(i)}\alpha_2^{-n_2(i)}N_0}{\rho_n 2K} = \frac{2^{-n}\alpha_1^{-n_1(i)}\alpha_2^{-n_2(i)}N_0}{[(1/2)(\alpha_1^{-1}+\alpha_2^{-1})]^n N_0} = \frac{\alpha_1^{n_2(i)}\alpha_2^{n_1(i)}}{(\alpha_1+\alpha_2)^n}. \quad (8.32)$$

We have

$$\mu([0,1]) = \sum_{i=1}^{2^n} \mu_i^{(n)} = 1.$$

The measures of the intervals $[0,1/2]$ and $[1/2,1]$ are given by

$$p = \mu_1^{(1)} = \frac{\alpha_2}{\alpha_1+\alpha_2}, \quad 1-p = \mu_2^{(1)} = \frac{\alpha_1}{\alpha_1+\alpha_2}, \quad (8.33)$$

which gives

$$\lambda_a = \frac{\alpha_2}{\alpha_1+\alpha_2}\ln\alpha_1 + \frac{\alpha_1}{\alpha_1+\alpha_2}\ln\alpha_2. \quad (8.34)$$

It can be checked that

$$\lambda_a \le \kappa, \quad (8.35)$$

where the equality holds if the vertical stretching is uniform across the unit interval in x: $\alpha_1 = \alpha_2$.

8.3.1.2 Dimension Formulas

For a general two-dimensional map with two positive Lyapunov exponents, $0 < \lambda_1^+ \le \lambda_2^+$, we have, from Sect. 8.2.2, $U = 2 = N$, $I = 0$, and $S = 0$, so that $D_{\mathrm{u},1} = 2$ and $D_{\mathrm{s},1} = D_1$. Depending on the value of κ relative to those of λ_2^+ and λ_1^+, there are two cases in which the dimension formula for D_1 is different. The first case is $\lambda_1^+ < K_1 < \lambda_2^+$, so $J = 1$ and we have

$$D_1 = D_{\mathrm{s},1} = 1 + \frac{K_1 - \lambda_1^+}{\lambda_2^+} = 2 - \frac{\kappa}{\lambda_2^+}. \quad (8.36)$$

The second case is $K_1 < \lambda_1^+$, so $J = 0$. In this case, the dimension is

$$D_1 = D_{\mathrm{s},1} = \frac{K_1}{\lambda_1^+} = 1 + \frac{\lambda_2^+}{\lambda_1^+} - \frac{\kappa}{\lambda_1^+}. \quad (8.37)$$

Because of the inequality (8.35), there are three distinct cases: (i) $\lambda_b > \kappa > \lambda_a$, (ii) $\kappa > \lambda_b > \lambda_a$, and (iii) $\kappa > \lambda_a > \lambda_b$, which should be treated separately. For illustrative purpose, we set $\alpha_2 = r\alpha_1$ and calculate how the dimension D_1 varies with the parameter α_1. We have

$$\begin{aligned}\kappa &= \ln 2 + \ln \alpha_1 - \ln(1 + r^{-1}),\\ \lambda_a &= \ln \alpha_1 + (1+r)^{-1} \ln r,\\ \lambda_b &= \ln 2.\end{aligned} \tag{8.38}$$

For case (i), the condition $\lambda_b > \kappa > \lambda_a$ stipulates that $\ln \alpha_1 < \ln(1 + r^{-1}) \equiv \ln \alpha_a$. The order of the Lyapunov exponents is then $\lambda_2^+ = \lambda_b > \lambda_1^+ = \lambda_a$. We have $\lambda_1^+ < K_1 < \lambda_2^+$ so that $J = 1$. Application of formula (8.36) gives

$$D_1 = 1 + \frac{\ln(1 + r^{-1}) - \ln \alpha_1}{\ln 2}, \quad \text{for } \alpha_1 < \alpha_a. \tag{8.39}$$

For case (ii), the defining condition $\kappa > \lambda_b > \lambda_a$ is equivalent to $\ln \alpha_a < \ln \alpha_1 < \ln 2 - (1+r)^{-1} \ln r \equiv \ln \alpha_b$. The order of the Lyapunov exponents is the same as in case (i). However, we now have $K_1 = \lambda_2^+ + \lambda_1^+ - \kappa < \lambda_1^+$ so that $J = 0$. The corresponding formula (8.37) thus gives

$$D_1 = \frac{(1+r)^{-1} \ln r + \ln(1 + r^{-1})}{\ln \alpha_1 + (1+r)^{-1} \ln r}, \quad \text{for } \alpha_a < \alpha_1 < \alpha_b. \tag{8.40}$$

For case (iii), we have $J = 0$ and $\ln \alpha_1 > \ln \alpha_b$. The order of the Lyapunov exponents is $\lambda_2^+ = \lambda_a > \lambda_1^+ = \lambda_b$, and (8.37) yields

$$D_1 = \frac{\ln(1 + r^{-1}) + (1+r)^{-1} \ln r}{\ln 2}, \quad \text{for } \alpha_1 > \alpha_b. \tag{8.41}$$

Results (8.39), (8.40), and (8.41) are summarized schematically in Fig. 8.2. We see that $D_1 > 1$ for $\alpha_1 < \alpha_a$ but $D_1 < 1$ for $\alpha_1 > \alpha_a$. In fact, for $\alpha_1 < \alpha_a$, the chaotic repeller, which is the basin boundary between the $y = \pm\infty$ attractors, is a fractal curve, as shown in Fig. 8.3. Numerical computation indicates [746] that for the repeller,

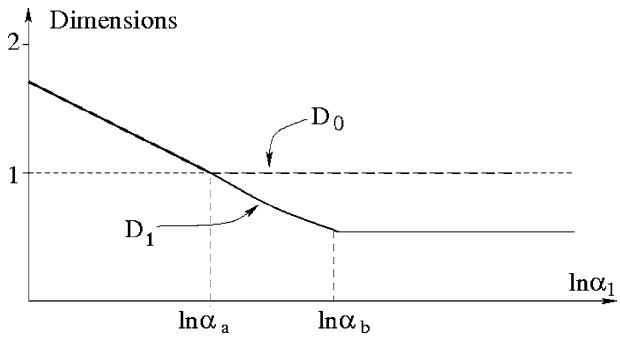

Fig. 8.2 For map (8.27), dimension of the chaotic repeller versus parameter α_1. For $\alpha_1 < \alpha_a$, the information dimension D_1 and the box-counting dimension D_0 of the chaotic repeller are greater than 1 and are equal. For $\alpha_1 > \alpha_a$, $D_1 < 1$, but $D_0 = 1$. Geometrically, there is a transition from a fractal to a nonfractal behavior in the basin boundary as α_1 is increased through α_a

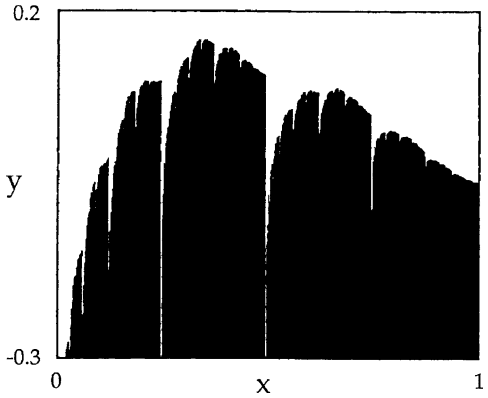

Fig. 8.3 For map (8.27), basins of attraction of the $y = +\infty$ (*blank*) and $y = -\infty$ (*black*) attractors for $\alpha_1 = 1.1$ and $r = 3$. The basin boundary, a chaotic repeller, is apparently a fractal curve. Both its box-counting and information dimensions are $D \approx 1.28$ [746] (with kind permission from Elsevier Science)

the box-counting dimension D_0 and the information dimension D_1 are equal. For $\alpha_1 > \alpha_a$, however, the repeller is a smooth curve with $D_0 = 1$. Geometrically, there is thus a transition from fractal to nonfractal behavior as α_1 is increased through α_a. Numerically obtained values of the information dimension of the repeller agree with those predicted by the formulas (8.40)–(8.41) [746]. For $\alpha_1 > \alpha_a$ the natural measure is rather irregular in spite of the fact that the support of the measure is a smooth curve.

8.3.1.3 The Issue of Typicality

The dimension formulas (8.21)–(8.25) were conjectured to apply for *typical* systems [347]. The two-dimensional map (8.27) provides a good example through which the notions of typicality and atypicality can be understood. In particular, consider $\eta = 0$. In this case, the line $y = 0$ is invariant in that a trajectory starting from this line remains on it forever. This invariant subspace, which is the x-axis, is the basin boundary in which the chaotic repeller resides. The natural measure is thus distributed on the x-axis. Dividing the x unit intervals into 2^n subintervals of width 2^{-n}, the measure contained in each subinterval is given by $\mu_i^{(n)}$ in (8.32). The information dimension of the natural measure for large n is (see (1.22))

$$D_1 = \frac{\sum_{i=1}^{2^n} \mu_i(n) \ln 1/\mu_i^{(n)}}{\ln 2^n}. \tag{8.42}$$

Utilizing (8.32) and the fact that for large n, the typical (most probable) values of n_1, n_2 are

$$\frac{n_1}{n} = \frac{\alpha_2}{\alpha_1 + \alpha_2}, \quad \frac{n_2}{n} = \frac{\alpha_1}{\alpha_1 + \alpha_2}, \tag{8.43}$$

we obtain the same expression for D_1 as in case (iii), (8.41). Thus for $\eta = 0$, the information dimension is a constant for all α_1 and $\alpha_2 > 1$. The dimension formulas yield, however, different results for different ranges of α_1. In particular, for $\lambda_a < \lambda_b$, they provide larger values than the exact information dimension (8.41). The situation $\eta = 0$ is thus *atypical*. However, as soon as we set $\eta \neq 0$, no matter how small, the dimension formulas are recovered and (8.41) becomes valid for $\alpha_1 > \alpha_b$ only. This is so because the value of $\eta \neq 0$ can always be scaled to one by the change of variable $y \to y/\eta$.

8.3.2 A Chaotic Billiard Scatterer

We consider a three-dimensional billiard scattering system with dynamics similar to those seen in the map example in the preceding discussion. As shown in Fig. 8.4a, the system consists of an ellipsoid placed in an infinite tube in the z-direction with cross section as shown in Fig. 8.4b. A free particle moving in the tube experiences elastic bounces off the walls of the tube and off the surface of the ellipsoid as well. Depending on the initial position and the initial velocity of the particle, it approaches either $z = +\infty$ or $z = -\infty$. The boundaries between these two exit basins are located near $z = 0$. Since the particle motion has three degrees of freedom, which corresponds to a phase-space dimension of five (due to energy conservation), the system represents a physical example in which high-dimensional chaotic scattering can arise and the dimension formulas can be tested in the typical setting whereby the ellipsoid is tilted slightly with respect to the z-axis. The symmetric system, in which the major axis of the ellipsoid is the z-axis, represents an atypical situation

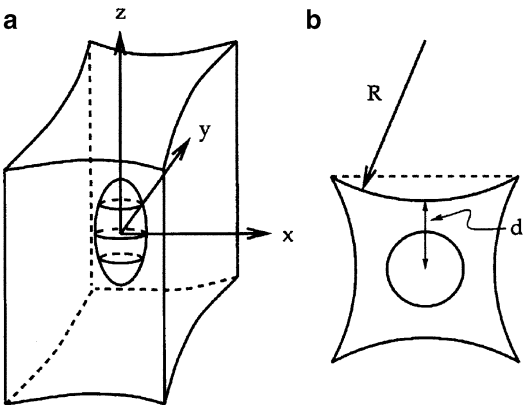

Fig. 8.4 (**a**) Billiard system consisting of an ellipsoid placed at $z = 0$ in an infinite tube in the z-direction. (**b**) Cross sections of the tube and of the billiard at $z = 0$. The parameters are $R = 25$, $d = 10$, and the radius of the ellipsoid at $z = 0$ is 5 [745, 746] (with kind permission from Elsevier Science)

whereby the dimension formulas could fail. This billiard system thus also represents an example in which the mathematical notions of typicality versus atypicality can be understood intuitively in physical terms.

To study the scattering dynamics, it is convenient to focus on bounces from the ellipsoid. Setting particles at the unit speed and utilizing cylindrical coordinates (z,ϕ) and (v_z,v_ϕ), Sweet and Ott derived a four-dimensional map relating these coordinates at a bounce to the previous one from the ellipsoid [745,746]. If the particle goes over the top (bottom) of the ellipsoid with $v_z>0$ ($v_z<0$), it continues toward $z=+\infty$ ($z=-\infty$). Due to the inward wall curvature of the tube, there is a sensitive dependence on initial conditions in the particle dynamics, signifying chaotic scattering. This can be seen explicitly by considering the symmetric case in which there is an invariant manifold Λ defined by $z=0$ and $v_z=0$ in the four-dimensional phase space, since particles started in Λ never leave it. The dynamics in the invariant manifold Λ is that of a two-dimensional billiard shown in Fig. 8.4b, which is hyperbolic and ergodic in the sense that almost every orbit comes arbitrarily close to any point in the phase space. The invariant set Λ is nonattracting in the four-dimensional phase space because almost all initial conditions in the vicinity of Λ lead to trajectories that go to $z=\pm\infty$. In particular, if a cloud of initial conditions is sprinkled in a region containing Λ, the fraction of trajectories that remain in this region up to n bounces decreases exponentially with time as $\sim\exp(-\kappa n)$, where κ is the escape rate. For typical trajectories with respect to the natural measure on Λ, there are two pairs of Lyapunov exponents, $\pm\lambda_\phi$ and $\pm\lambda_z$, which characterize motions on the chaotic set and toward or away from it, respectively. The scattering dynamics is thus chaotic with two positive Lyapunov exponents, and numerically the inequality $\lambda_\phi>\lambda_z$ has been found [745,746]. In this special configuration, the full manifold Λ is a chaotic saddle.

For the case in which the ellipsoid is slightly tilted, the saddle survives, but its geometry becomes more complicated. The Lyapunov exponents for typical trajectories with respect to the natural measure on the saddle are, however, approximately the same as those in the untilted case.

The stable manifold of the saddle is physically important because it separates the space of initial conditions into two regions that yield trajectories approaching $z=\pm\infty$, respectively. These regions, the exit basins, can be determined numerically, as shown in Fig. 8.5a, b for the untilted and slightly tilted cases, respectively, which represent two-dimensional cross sections in the four-dimensional map. A straightforward application of the dimension formulas (8.21) and (8.24) with $U=S=2$ in this typical case yields

$$D_{\mathrm{s},1}=D_{\mathrm{u},1}=4-\frac{\kappa}{\lambda_\phi},\quad D_1=4-2\frac{\kappa}{\lambda_\phi},\quad \text{for } \lambda_\phi>\kappa, \tag{8.44}$$

where $J=1$. For $\lambda_\phi<\kappa$ so that $J=0$, we have

$$D_{\mathrm{s},1}=D_{\mathrm{u},1}=3-\frac{\kappa-\lambda_\phi}{\lambda_z},\quad D_1=2-2\frac{\kappa-\lambda_\phi}{\lambda_z}. \tag{8.45}$$

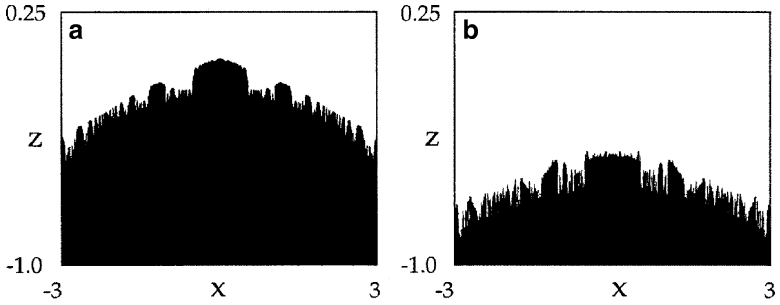

Fig. 8.5 Examples of regions of initial conditions (*exit basins*) that yield trajectories to $z \to +\infty$ (*white*) and $z \to -\infty$ (*black*) in the two-dimensional cross section (x, z) defined by $y = 5.1$, $v_x = 0$, and $v_z = 0.1$ for (**a**) the untilted case and (**b**) a small tilt of $2\pi/100$ [745,746] (with kind permission from Elsevier Science)

Note that in this second case the information dimension of the manifold (saddle) is less than 3 (2). When plotting these dimensions as a function of κ/λ_ϕ one would see a break at 3 (2), similar to that seen in Fig. 8.2 at α_a.

For the untilted (atypical) case, a detailed analysis [746] gives that the dimension is

$$D_{\mathrm{s},1} = D_{\mathrm{u},1} = 4 - \frac{\lambda_z + \kappa}{\lambda_\phi}, \quad D_1 = 4 - 2\frac{\lambda_z + \kappa}{\lambda_\phi}, \quad \text{for } \lambda_\phi > \lambda_z + \kappa. \tag{8.46}$$

The meanings and relationship between the above two dimension formulas can be understood as follows. Suppose one uses some algorithm to compute the dimension with refining accuracy ε. Then for an infinitesimal amount of tilt the true value of the dimension as given by (8.44) can be obtained only when ε is small, e.g., for $\varepsilon < \varepsilon_*$. For resolution size greater than ε_*, the small amount of tilt has no effect, so that the value of the dimension extracted for $\varepsilon > \varepsilon_*$ would agree with that given by (8.46). Around ε_*, the scaling with ε is expected to show a crossover from the form given by (8.46) to that given by (8.44). In a physical experiment with a finite resolution of distance scales, if the amount of tilt is small, the measured dimension may be that given by (8.46). The true dimension can be recovered only in the $\varepsilon \to 0$ limit.

Note that since the stable manifold of the saddle divides the four-dimensional phase space, its *box-counting* dimension is at least three. Numerically, it was found [746] that in the tilted and untilted configurations the stable manifold's box-counting dimensions are close to the information dimensions predicted by formulas (8.44) and (8.46), respectively, insofar as these dimensions are larger than 3, as shown in Fig. 8.6. Otherwise, the box-counting dimensions were found to remain at 3. The two dimensions deviate here drastically, similar to the situation in the $\alpha > \alpha_a$ range of Fig. 8.2.

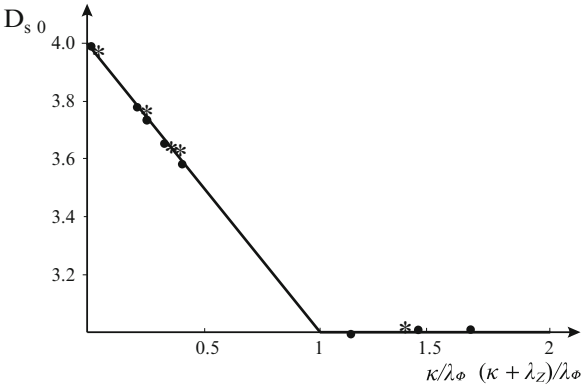

Fig. 8.6 Numerical verification of the stable manifold's dimension for the tilted case (variable κ/λ_ϕ) and the untilted case (variable $(\kappa+\lambda_z)/\lambda_\phi$). The linear curve corresponds to formulas (8.44) and (8.46) for $D_{s,1} > 3$. Dots (*stars*) represent numerically determined values of the box-counting dimension $D_{s,0}$ for the tilted (*untilted*) case

8.4 Numerical Method for Computing High-Dimensional Chaotic Saddles: Stagger-and-Step

8.4.1 Basic Idea

In applications involving transient chaos, it is often useful and desirable to detect and compute chaotic saddles. Several methods have been described in Chap. 1, but they are applicable to systems with *one unstable direction only*. To numerically construct chaotic saddles in higher dimensions with more than one unstable direction, two methods are presently available. One is the "PIM-simplex" method by Moresco and Dawson [529] and another is the "stagger-and-step" method by Sweet et al. [744]. The PIM-simplex method is relatively sophisticated, and its applicability is somewhat limited [529, 744]. The stagger-and-step method is, however, relatively straightforward to implement and it is generally applicable to chaotic saddles that are unstable in several dimensions. Here we focus on this method.

Consider an N-dimensional continuous map $\mathbf{f}$, where $N \geq 2$, and assume that a chaotic saddle exists within a restraining region Γ that does not contain any attractor. The transient lifetimes for initial conditions in Γ can be defined as follows. For initial condition $\mathbf{x}$, the escape time $T(\mathbf{x})$ is the minimum $n \geq 0$ for which the nth iterate is in Γ but the $(n+1)$th iterate of $\mathbf{x}$ is not in Γ. For points $\mathbf{x}$ on the stable manifold of the chaotic saddle in Γ, the escape time is $T(\mathbf{x}) = \infty$. If $T(\mathbf{x})$ is finite but large, $\mathbf{x}$ is close to the stable manifold. That is, all points with escape time at least n, where n is large, belong to a small neighborhood of the stable set. This observation is the main idea behind the stagger-and-step method.

A *stagger* is a perturbation $\mathbf{r}$ to a point $\mathbf{x}$ that results in a new point $\mathbf{x}+\mathbf{r}$ such that $T(\mathbf{x}+\mathbf{r}) > T(\mathbf{x})$. The stagger method generates sequences $\{\mathbf{x}_n\}$ of the form

$\mathbf{x}_{n+1} = \mathbf{x}_n + \mathbf{r}_n$, where $\mathbf{r}_n$ is a stagger, such that $T(\mathbf{x}_{n+1}) > T(\mathbf{x}_n)$. Such sequences are called stagger trajectories. The purpose is to find a point or a small set of points that are sufficiently close to the stable manifold. To do so, one can specify some relatively large $\delta > 0$. Starting from $n = 0$, for each n, random perturbations $\mathbf{r}$ of magnitude less than δ are repeatedly chosen using some specified probability distribution until one with $T(\mathbf{x}_n + \mathbf{r}) > T(\mathbf{x}_n)$ is found. One can then set $\mathbf{r}_n = \mathbf{r}$. The process stops as soon as $T(\mathbf{x}_{n+1}) > T^*$, where T^* is a predetermined (large) time. Sometimes δ may be too small so that no stagger can be found. In this case, one should increase δ.

In order to guarantee that stagger trajectories can be found in an efficient way, the probability distribution from which $\mathbf{r}$ is chosen is important. A uniform distribution, for instance, is not a good choice because the fraction of perturbations that are staggers goes to zero exponentially fast as the escape time increases. This is a consequence of the general exponential decay of transiently chaotic systems. To overcome this difficulty, Sweet et al. suggested using an "exponential stagger distribution" for choosing $\mathbf{r}$, which can be realized as follows. Write $10^{-a} = \delta$ and let s be a uniformly distributed random variable between a and b, where 10^{-b} is the accuracy of double precision in digital computers (typically $b = 15$). The choice of $\mathbf{r}$ is thus $\mathbf{r} = 10^{-s}\mathbf{u}$, where $\mathbf{u}$ is a random directional unit vector. In so doing, the fraction of staggers decreases much more slowly than exponentially, and hence the probability of finding a stagger can be enhanced significantly as compared with the case of uniform distribution, thereby reducing the computation time.

After a stagger trajectory is found, a point $\mathbf{x}_0$ can be picked up for which $T(\mathbf{x}_0) > T^*$. One can then generate a trajectory $\{\mathbf{x}_n\}$ using the map $\mathbf{f}$. The basic idea is to apply the map only when $\mathbf{x}_n$ has escape time $T(\mathbf{x}_n) > T^*$. If $T(\mathbf{x}_n) \le T^*$, then one finds a nearby stagger point $\mathbf{x}_n + \mathbf{r}_n$ with a higher escape time using $\delta = \varepsilon$ (say 10^{-10}). The trajectory $\{\mathbf{x}_n\}$ is of the form

$$\mathbf{x}_{n+1} = \begin{cases} \mathbf{f}(\mathbf{x}_n) & \text{if } T(\mathbf{x}_n) > T^* \text{ (a step)}, \\ \mathbf{f}(\mathbf{x}_n + \mathbf{r}_n) & \text{if } T(\mathbf{x}_n) \le T^* \ (\mathbf{r}_n \text{ is a stagger}), \end{cases} \tag{8.47}$$

where $|\mathbf{r}_n| \le \varepsilon$ and $T(\mathbf{x}_n + \mathbf{r}_n) > T(\mathbf{x}_n)$. (Note that $T[\mathbf{f}(\mathbf{x}_n)] = T(\mathbf{x}_n) - 1$.) Such a trajectory is called a *stagger-and-step* trajectory. By construction, any stagger-and-step trajectory $\{\mathbf{x}_n\}$ satisfies $|\mathbf{f}(\mathbf{x}_n) - \mathbf{x}_{n+1}| < \varepsilon$, so that $\{\mathbf{x}_n\}$ is a numerical trajectory with precision of order $\varepsilon = 10^{-10}$, and it is close to the chaotic saddle after a few iterates. From a stagger-and-step trajectory, dynamical invariants such as the Lyapunov exponents of the saddle can be computed.

To give an example, Sweet et al. [744] considered the following four-dimensional map:

$$\begin{aligned} x_{n+1} &= A - x_n^2 + By_n + k(x_n - u_n), \\ y_{n+1} &= x_n, \\ u_{n+1} &= C - u_n^2 + Dv_n + k(u_n - x_n), \\ v_{n+1} &= u_n, \end{aligned} \tag{8.48}$$

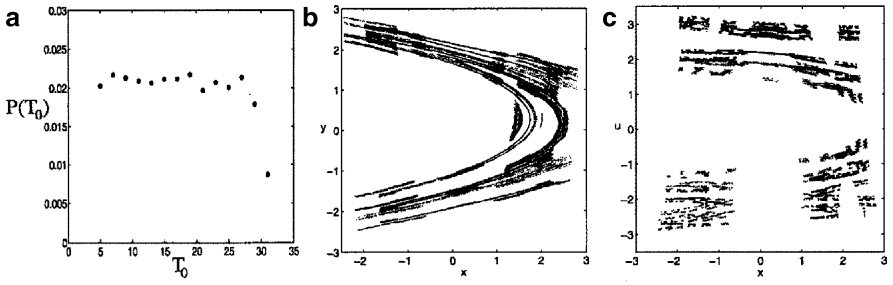

Fig. 8.7 Stagger-and-step method. (**a**) An example of the probability of finding a stagger versus the escape time, (**b**, **c**) projections of a trajectory of 10^5 points of the chaotic saddle, for the four-dimensional map (8.48) at the set of parameter values given in the text [744] (copyright 2001, the American Physical Society)

where A, B, C, D, and k are parameters. For $A = 3.0$, $B = 0.3$, $C = 5.0$, $D = 0.3$, and $k = 0.4$, there is transient chaos. The restraining region Γ was chosen to be $(-4,4) \times (-4,4) \times (-4,4) \times (-4,4)$ and δ to be the length of the diagonal of Γ ($\delta = 16$). To find a stagger required about 50 choices of perturbed points $\mathbf{r}$, the probability of which is approximately 0.02, at least for a range of the escape time, as shown in Fig. 8.7a. It can be seen that for escape time T_0 between 5 and 29, this probability is indeed approximately constant. The projections of a stagger-and-step trajectory of 10^5 points on the chaotic saddle in the (x,y)-plane and in the (x,u)-plane are shown in Fig. 8.7b and c, respectively, where $\varepsilon = 10^{-10}$ and $T^* = 30$. From this trajectory the Lyapunov exponents of the chaotic saddle were computed to be $\lambda_2^+ \approx 1.33$, $\lambda_1^+ \approx 0.77$, $\lambda_1^- \approx 1.97$, and $\lambda_2^- \approx 2.54$.

The stagger-and-step method slows down with increasing dimensionality due to the exponential growth of phase-space volume with dimension. A recent method due to Bollt [87] replaces the random choice by a deterministic search for larger lifetimes. To this end, one determines the lifetime function in the phase space. For any point one can then find the direction along which the lifetime increases the fastest. This gradient-search algorithm leads to solving an ordinary differential equation, which essentially follows the unstable foliation toward the stable manifold of the chaotic saddle. The method has been shown to be efficient for maps of dimension at least eight.

8.4.2 Invariant Sets Constrained to Slow Manifolds

In high-dimensional systems one is often faced with the problem of the separation of time scales. In such multiscale systems the fast, high-frequency components damp out rapidly due to dissipation, and the dynamics becomes restricted to a lower-dimensional manifold embedded in the full phase space. This manifold is called the *slow manifold*, the dynamics on which may turn out to be transiently chaotic. Morgan, Bollt, and Schwartz [530] worked out a method to determine invariant sets in slow manifolds.

A paradigmatic form of multiscale systems is given by the differential equations

$$\begin{aligned} \dot{\mathbf{x}} &= \mathbf{F}(\mathbf{x}, \mathbf{y}; \mu), \\ \mu \dot{\mathbf{y}} &= \mathbf{G}(\mathbf{x}, \mathbf{y}; \mu), \end{aligned} \tag{8.49}$$

where $\mu \ll 1$ is a small parameter characterizing the separation in time scales, and the vector $\mathbf{y}$ denotes the fast variables. In the limit of extreme separation, $\mu = 0$, (8.49) reduces to an algebraic constraint: $\mathbf{G}(\mathbf{x}, \mathbf{y}, 0) = 0$. Solving the constraint for $\mathbf{y}$ yields an expression $\mathbf{y} = \mathbf{H}_0(\mathbf{x})$. The graph of $\mathbf{H}_0$ is the slow manifold in this limit, assumed to be single-valued for simplicity. The dynamics on the slow manifold is obtained from (8.49) as

$$\dot{\mathbf{x}} = \mathbf{F}[\mathbf{x}, \mathbf{H}_0(\mathbf{x}); 0]. \tag{8.50}$$

For nonzero but small values of μ, the slow manifold is expected to persist. It is given by the graph of a function labeled as $\mathbf{y} = \mathbf{H}_\mu(\mathbf{x})$, which can be obtained as an expansion in powers of μ starting with $\mathbf{H}_0(\mathbf{x})$. The dynamics on this slow manifold can also be obtained from a perturbation expansion starting with (8.50). For a suitably defined map, the full dynamics can be written as $(\mathbf{x}_{n+1}, \mathbf{y}_{n+1}) = \mathbf{f}(\mathbf{x}_n, \mathbf{y}_n)$, and the form of the slow manifold is $\mathbf{y}_n = \mathbf{H}_\mu(\mathbf{x}_n)$.

In order to construct the chaotic saddle on the slow manifold, Morgan et al. [530] applied the stagger-and-step method with the following modifications. The restraining region Γ is chosen as a neighborhood of the slow manifold. Since orbits can enter this region, one looks for the first escape time from Γ. The step-and-stagger iterations are chosen as

$$(\mathbf{x}_{n+1}, \mathbf{y}_{n+1}) = \begin{cases} \mathbf{f}[\mathbf{x}_n, H_\mu(\mathbf{x}_n)] & \text{(a step)}, \\ \mathbf{f}[\mathbf{x}_n + \mathbf{r}_n, H_\mu(\mathbf{x}_n + \mathbf{r}_n)] & \text{(a stagger)}, \end{cases} \tag{8.51}$$

and the iterate $\mathbf{y}_{n+1}$ is projected back onto the slow manifold, so that the resulting stagger-and-step trajectory lies near the slow manifold. In addition, since the slow manifold is determined with finite precision (typically a power of μ), the parameter δ that sets the modulus of the stagger perturbation cannot be chosen to be less than this accuracy.

The method has been successfully applied to a structural mechanical system in [530] with two slow variables ψ_1, ψ_2. Figure 8.8 shows the chaotic saddle projected on the plane of the slow variables.

A more complete picture can be obtained by plotting the slow manifold along with the stable and unstable foliations on it. In the spirit of the sprinkler method (Sect. 1.2.2.3), an approximation of these manifolds can be obtained by searching for trajectories that remain near the slow manifold (and do not approach any attractor) for sufficiently long times. The initial points of such trajectories approximate the stable manifold. The unstable manifold can be obtained, e.g., by applying the same procedure to the time-reversed dynamics. The algorithm is called the constrained invariant-manifold method. Figure 8.9 shows a case in which for simplicity, there is

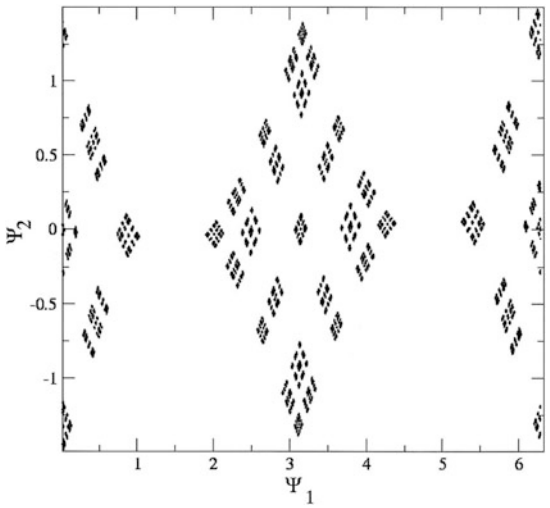

Fig. 8.8 Result of the modified stagger-and-step algorithm (8.51) applied to the problem of a pendulum coupled to a viscoelastic rod. The chaotic saddle is shown on a stroboscopic map in the plane of the slow variables ψ_1, ψ_2. The time-scale parameter is $\mu = 0.05$, and the slow manifold is specified with an accuracy of μ^2 [530] (copyright 2003, the American Physical Society)

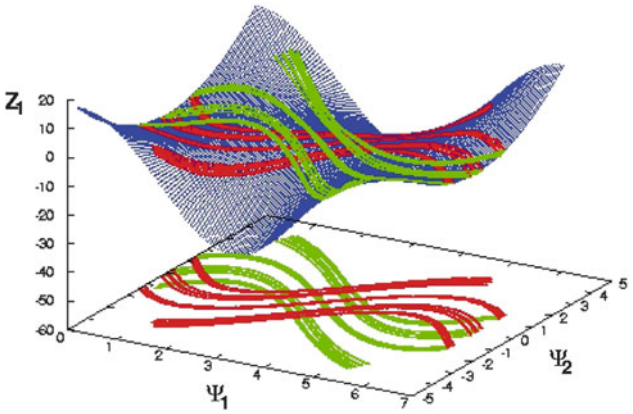

Fig. 8.9 The slow manifold $z_{1,n} = H_\mu(\psi_{1,n}, \psi_{2,n})$ (*blue*) in the problem of a pendulum coupled to a viscoelastic rod as it appears on a stroboscopic map at the parameters of Fig. 8.8. The stable (*unstable*) manifold is plotted in *green* (*red*) [530] (copyright 2003, the American Physical Society)

a single fast variable z_1. The slow manifold is a smooth surface in the phase space of one fast and two slow variables. The invariant manifolds are given both in the slow manifold and in the plane of the slow variables.

8.5 High-Dimensional Chaotic Scattering

As a physical manifestation of high-dimensional transient chaos, we discuss a class of three-degree-of-freedom, time-independent open Hamiltonian systems that exhibit chaotic scattering. Issues to be addressed are the dimension requirement for chaotic scattering to be physically observed and the topology of high-dimensional chaotic scattering. While there have been attempts to address chaotic scattering in higher-dimensional systems [124, 366, 444, 745–748, 829], the topic is relatively unexplored and much research is needed.

8.5.1 Dimension Requirement for Chaotic Saddles to be Observables

Due to the high dimensionality of the phase space, an issue of concern is whether chaotic scattering can be observed even if there is a chaotic saddle of low dimension in the scattering region. In particular, suppose in a scattering experiment, one measures a scattering function for particles launched from a one-dimensional line segment. If the dimension of the chaotic saddle is not sufficiently high, its stable manifold may not have generic intersections with the line. Such intersections, and consequently a set of singularities in the scattering function, can be observed only when the dimension of the chaotic saddle is sufficiently high.

To address this observability issue, we recall a basic mathematical statement concerning the dimension of the intersection between two sets. Let S_1 and S_2 be two subsets of an N-dimensional manifold with dimensions $D(S_1)$ and $D(S_2)$, respectively. The dimension of the set of intersection between S_1 and S_2 is denoted by $D(S_1 \bigcap S_2)$. The question is whether the sets S_1 and S_2 intersect generically in the sense that the intersection cannot be removed by small perturbations. The natural approach is to look at the dimension D_I:

$$D_I = D(S_1) + D(S_2) - N.$$

If $D_I \geq 0$, the intersection is generic, and the dimension of the set of intersection is [232]

$$D(S_1 \bigcap S_2) = D_I = D(S_1) + D(S_2) - N. \tag{8.52}$$

If D_I is negative, then S_1 and S_2 do not have a generic intersection. For example, consider the intersection between two one-dimensional curves in a two-dimensional plane: $D(S_1) = D(S_2) = 1$ and $N = 2$. We obtain $D_I = 0$, which means that the intersecting set consists of points, and the intersections are generic because small perturbations cannot remove them. If, however, $N = 3$, then $D_I < 0$, which means that two one-dimensional curves do not intersect generically in a three-dimensional space. If they intersect at a point, small perturbations in the positions of the lines typically remove the intersection. These two cases, together with an additional one

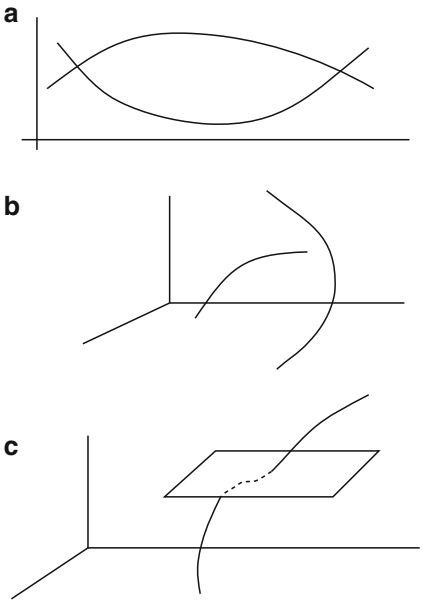

Fig. 8.10 Illustration of generic and nongeneric intersections of simple geometric sets: (**a**) $D_1 = D_2 = 1$ and $N = 2$ (generic intersection), (**b**) $D_1 = D_2 = 1$ and $N = 3$ (nongeneric intersection), and (**c**) $D_1 = 1$, $D_2 = 2$, and $N = 3$ (generic intersection)

($D(S_1) = 1$, $D(S_2) = 2$, and $N = 3$), are illustrated in Fig. 8.10. It can also be said that the codimension $D - N$ is additive for generically intersecting sets. Formula (8.52) is valid for both the box-counting and the information dimensions.

To apply these arguments to chaotic scattering, we consider a continuous-time autonomous scattering system of phase-space dimension $N + 2$. Due to energy conservation, the corresponding continuous-time flow is $(N + 1)$-dimensional, so the scattering map is N-dimensional. The box-counting dimensions of the stable and the unstable manifolds in the map are denoted by $D_{s,0}$ and $D_{u,0}$. The symplectic nature of the dynamics stipulates $D_{u,0} = D_{s,0}$. The box-counting dimension of the chaotic saddle is

$$D_0 = D_{s,0} + D_{u,0} - N = 2D_{s,0} - N, \tag{8.53}$$

since dynamically, the chaotic saddle is the intersecting set between the stable and the unstable foliations. Let $0 < d_s \leq 1$ be the box-counting dimension of the singularities probed by a scattering function. This is the set of intersecting points between the stable manifold of dimension $D_{s,0}$ and a one-dimensional line segment from which particles are initiated in the N-dimensional map. Equation (8.52) implies

$$d_s = D_{s,0} + 1 - N, \tag{8.54}$$

or $D_{s,0} = d_s + N - 1$. Utilizing (8.53) gives the following formula relating the dimension of the chaotic saddle to d_s:

$$d_s = \frac{D_0 - N + 2}{2}. \tag{8.55}$$

Scattering singularities can be seen if $d_s > 0$, which is fulfilled only if

$$D_0 > N - 2. \tag{8.56}$$

For a two-degree-of-freedom autonomous Hamiltonian system, one obtains a two-dimensional map, $N = 2$, so the condition is always satisfied. In contrast, in a three-degree-of-freedom system, $N = 4$, and D_0 must be larger than 2 for chaotic scattering to be observable. In this case, if the box-counting dimension of the saddle in the map is smaller than 2, the set of singularities will not be observable, and as a result, any measured scattering function will typically exhibit only smooth features. This implies that by examining the scattering functions only, no chaotic behavior can be revealed, even when there is a chaotic saddle in the phase space and the scattering dynamics is chaotic.

8.5.2 *Normally Hyperbolic Invariant Manifolds in High-Dimensional Chaotic Scattering*

For high-dimensional scattering systems, hyperbolic periodic orbits and their stable and unstable manifolds often do not have the necessary dimensionality to partition the phase space on the energy shell. In search of higher-dimensional structures with features of periodic orbits of low-dimensional scattering, Wiggins and coworkers [808, 811, 829] suggest the geometrical objects of *normally hyperbolic invariant manifolds* [828]. On such a manifold, the expansion and contraction rates for the invariant motion are dominated by those transverse to the manifold. Like a saddle point, a normally hyperbolic invariant manifold has its own stable and unstable manifolds. In Hamiltonian systems, normally hyperbolic invariant manifolds can exist about equilibrium points of saddle-center-$\cdots$-center type. In an n-degree-of-freedom time-continuous system, such an equilibrium point possesses a pair of real eigenvalues of opposite signs (say $\pm\lambda$) and $2n-2$ purely imaginary eigenvalues occurring in complex conjugate pairs ($\pm i\omega_j$, $j = 2, \ldots, n$). In the $(2n-1)$-dimensional energy shell, the normally hyperbolic invariant manifold is a $(2n-3)$-dimensional sphere around the saddle-center-$\cdots$-center type of fixed point.

Normally hyperbolic invariant manifolds are typical in systems with internal degrees of freedom where some basic "transformation" can take place during the scattering process. Chemical reactions provide a natural example in this context. The basic transformation is then that reactants form products. The normally hyperbolic invariant manifold is the energy surface of an unstable invariant subsystem

with one degree of freedom less than that of the full system. In the terminology of chemistry, this subsystem is an activated complex, or an unstable supermolecule [808]. This unstable subsystem is thus a proper generalization of the basic hyperbolic periodic orbits in two-degree-of-freedom systems (e.g., the orbits bouncing between two disks in the three-disk scattering system; see Fig. 6.4). The activated complex or the normally hyperbolic invariant manifold is located between reactants and products. More precisely, around the normally hyperbolic invariant manifold the phase space has the "bottleneck" property that facilitates the construction of a dividing surface. This surface has the property of "no-recrossing" and therefore separates the phase-space region of reactants and products. The dividing surface is of dimension $2n-2$ and contains as an invariant set the intermediate complex.

The stable and the unstable manifolds of the intermediate complex are $(2n-2)$-dimensional, which is one dimension less than that of the energy surface. These manifolds can therefore act as *separatrices*, i.e., they enclose volumes of the energy shell. Their key dynamical significance is that the only way for trajectories to lead to reactions is for them to be in certain volumes enclosed by the stable and the unstable manifolds. Note that any Poincaré section of the continuous dynamics in the $(2n-1)$-dimensional energy shell defines an $(N=2n-2)$-dimensional map. The normally hyperbolic invariant manifold is an $(N-2)$-dimensional object in this map. Its stable and unstable manifolds have dimension $N-1$.

The stable and the unstable manifolds of the intermediate complex can cross each other. The homoclinic and heteroclinic intersections, as well as such intersections of subsets of the normally hyperbolic invariant manifolds, can then form a high-dimensional chaotic saddle.

If the chaotic saddle is formed by the intersections of the separatrix manifolds of the intermediate complex, the scattering functions are similar to those in low-dimensional systems. The locally $(N-1)$-dimensional manifolds have, with finite probability, intersections with any line of initial conditions: applying (8.52) with $D(S_1)=N-1$, $D(S_2)=1$ to get $D(S_1 \bigcap S_2)=0$, we see that the typical intersections are points. Furthermore, in such cases the chaotic saddle's full stable (unstable) manifold has box-counting dimension $> N-1$. As a consequence, the saddle, that is the intersection of these manifolds, is of dimension $D_0 > N-2$. Equation (8.55) gives then $d_s > 0$, implying that *the set of singularities is always observable* if the saddle is formed by normally hyperbolic invariant manifolds. The intersections of the stable manifold with a line yield the endpoints of intervals of continuity in the scattering function. They can thus be used to define scattering cross sections (Appendix D).

Besides chemical reactions, normally hyperbolic invariant manifolds have been applied to problems of celestial mechanics [806, 807] and to escape problems from multidimensional potential wells [809]. It is likely that the concept can have a broad range of potential applications in other contexts. A recent review of both the classical and quantum aspects of such transition-state theories can be found in [810].

8.5.3 Metamorphosis in High-Dimensional Chaotic Scattering

A prototype system for investigating high-dimensional chaotic scattering is the configuration in which scattering centers are located at the vertices of a regular tetrahedron [124, 444, 747, 748]. When the centers are hard-wall spheres [58, 124, 415, 535, 817], the problem corresponds to a light beam bouncing back and forth among reflecting balls that can be found, for instance, in holiday decorations. This type of chaotic scattering can be readily observed, and experiments have been carried out, generating fractal images [747, 748]. While the hard-wall system is illuminating for demonstrating the fractal structure associated with chaotic scattering in high dimensions, the topology of the scattering is fixed, analogous to the planar three-hard-disk scattering system. Basic issues such as bifurcations cannot be addressed using the hard-wall systems.

Because of this difficulty, scattering systems consisting of physically realistic *soft* potentials were considered [421, 444], which are relevant to the scattering of particles by molecules in the three-dimensional physical space. It was found [444] that (1) the chaotic-scattering topology can undergo a sudden change (*metamorphosis*) as a system parameter (e.g., energy) changes continuously, (2) at the metamorphosis, the behavior of the box-counting dimension of the chaotic saddle changes characteristically, and (3) chaotic scattering can occur in energy regimes for which it is not possible in the corresponding planar scattering system. An exemplar system consists of four potential hills located at the four vertices of a regular tetrahedron of unit side length, as shown in Fig. 8.11. To mimic physical situations such as particle scattering by nonrotating diatomic molecules, the Morse potential was chosen for each hill [444]. The total potential of the scattering system is

$$V(\mathbf{x}) = \sum_{j=1}^{4} V_M(\mathbf{x}, \mathbf{x}_j), \tag{8.57}$$

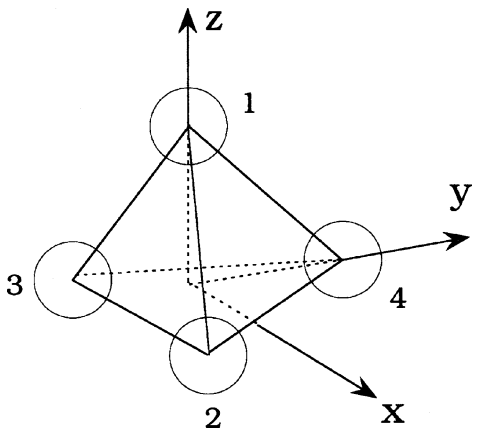

Fig. 8.11 A schematic illustration of the scattering system: four Morse potential hills located at the vertices of a regular tetrahedron [444] (copyright 2000, the American Physical Society)

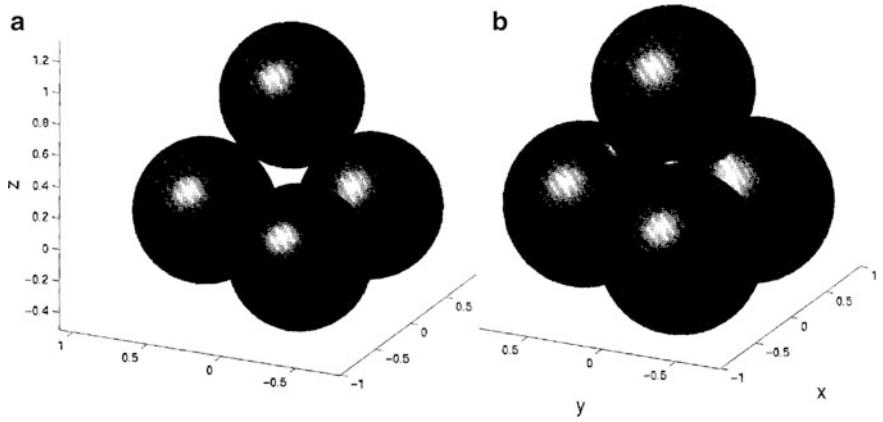

Fig. 8.12 Surfaces of equal energy for potential (8.57), for energies above and below the critical energy E_c. (**a**) Isoenergy surface for $E = 4$ ($E > E_c$); (**b**) Isoenergy surface for $E = 1$ ($E < E_c$) [444] (copyright 2000, the American Physical Society)

where $V_M(\mathbf{x}, \mathbf{x}_j)$ is given by (6.19), $\mathbf{x}_j$ ($j = 1, \ldots, 4$) denote the vertices of the tetrahedron, and $r_j = \sqrt{(x-x_j)^2 + (y-y_j)^2 + (z-z_j)^2}$ is the distance to vertex j. The particle energy E is a convenient bifurcation parameter.

The region of the three-dimensional physical space classically inaccessible to particles of energy E is given by $V(\mathbf{x}) > E$. In order to have chaotic scattering, the particle energy needs to be below the maximum energy E_m of the potential hills. For energy values larger than a critical energy E_c (and lower than E_m), the inaccessible part of the physical space consists of four disconnected regions, each surrounding one vertex of the tetrahedron, as shown in Fig. 8.12a. The regions are approximately spherical in shape, but are not perfectly spherical because their shapes are distorted by the other hills. As the energy decreases toward E_c, the inaccessible regions grow in radius, and for $E = E_c$, the previously disconnected regions begin to connect with each other. For $E \leq E_c$, the inaccessible regions are thus fully connected, as shown in Fig. 8.12b. As E is decreased from E_c, a whole family of orbits in the invariant set is destroyed. These are orbits that bounce back and forth between each pair of forbidden regions an arbitrary number of times, including the six unstable periodic orbits that connect each pair of hills existing for $E > E_c$. As these orbits are destroyed, however, another family of orbits is created at $E = E_c$; these orbits bounce off the newly created forbidden regions connecting each pair of hills. This topological change in the dynamics of the system at E_c can cause a metamorphosis in the scattering dynamics [444].

The basic physics associated with the topological metamorphosis can be understood in terms of the structural change in the "holes" on each side plane of the tetrahedron potential configuration as the particle energy is decreased. Each side plane of the tetrahedron potential (see Fig. 8.13) is similar to the two-dimensional

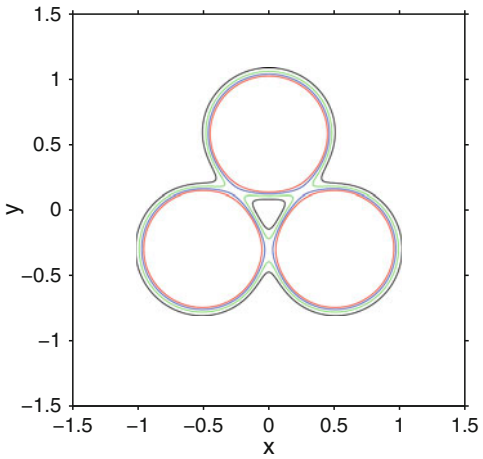

Fig. 8.13 Energy contours of the Morse potential in the (x, y)-plane at $z = 0$. The contours belong to the energy values $E = 4$ (*red*), $E = 3$ (*blue*), $E = 2$ (*green*), and $E = 1$ (*black*). Other parameters are $\alpha = 6$ and $r_e = 0.68$. The value of the critical energy is $E_c = 2.25$ [444] (copyright 2000, the American Physical Society)

system treated in Sect. 6.3.4. The critical energy E_c is close to the value of E_0 determined in the two-dimensional case. It was found numerically [444] that $E_c \approx 2.25$. For $E < E_c$, the forbidden regions are connected, and an incoming particle can penetrate the interior of the tetrahedron only through the holes on the side planes. The holes in the central regions of the side planes are always present, because of the attractive parts of each Morse hill. This allows particles to enter the scattering region inside the tetrahedron at low energies. For E slightly below E_c, the holes are relatively large, and hence the range of initial conditions with which particles can enter the holes are appreciable. The holes, however, become smaller as E is decreased further from E_c. For E slightly below E_c, the size of the hole can be estimated as

$$s \approx s_0 - C(E_c - E), \tag{8.58}$$

where $s_0 = (\sqrt{3} - 1)/2$ is the size for $E = E_c$ and C is a positive constant. Thus, to observe chaotic scattering at low energies in an experimental setting, initial conditions have to be prepared carefully so that particles can enter the holes, since the scattering will not be chaotic if the particles do not enter the holes. In fact, no unstable periodic orbit can be formed outside the holes for $E < E_c$.

To explore the scattering function, we note that, since the physical space is three-dimensional, there are two angles characterizing the momentum of a scattering particle: the azimuthal angle ϕ and the polar angle θ. Figure 8.14a, b show, for $E = 4$ and $E = 1$ respectively, ϕ after the scattering versus b, where particles are launched upward with $v_{x0} = v_{y0} = 0$, $v_{z0} = \sqrt{2E}$ from $z_0 = -10.0$, and the deflection angle $\phi(x_0)$ is recorded when the particles exit the scattering region. A Cantor set of singularities in the scattering dynamics implies the presence of a chaotic saddle whose

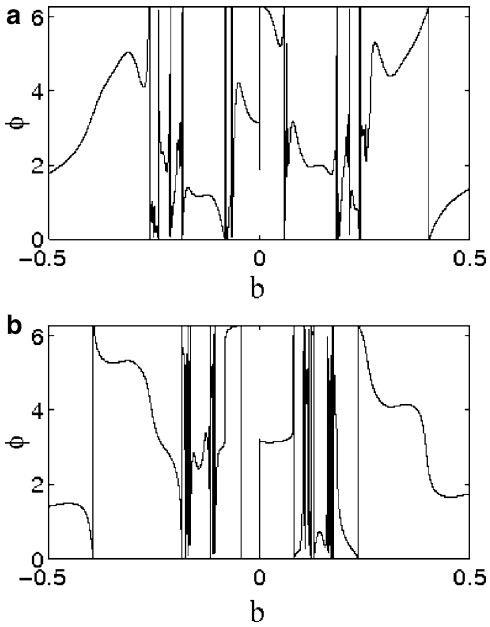

Fig. 8.14 Deflection function: azimuthal angle ϕ as a function of the impact parameter for (**a**) $E = 4$, and (**b**) $E = 1$ [444] (copyright 2000, the American Physical Society)

box-counting dimension in the underlying four-dimensional map is larger than two. The dynamical and physical natures of the scattering observed at these energies are, however, quite different, because of the topological change in the structure of the invariant set. A computation of the dimension d_s of the set of singularities in the scattering function leads, by (8.55) to the box-counting dimension D_0 of the chaotic saddle. It was found [444] that for $E = 4$, the dimension is $D_0 = 3.33 \pm 0.02$, and for $E = 1$, $D_0 = 2.83 \pm 0.02$. Figure 8.15 shows the dimension D_0 of the saddle versus E for $1 \leq E \leq 4$. For $E > E_c$, the dimension remains roughly constant. This is due to the structural stability of the chaotic saddle in this energy regime, where the potential hills remain isolated and hence there is no exponential change in the number of unstable periodic orbits. For $E < E_c$, D_0 appears to decrease as E is lowered from E_c.

The reason that the box-counting dimension decreases as the energy is decreased from E_c can be understood heuristically as follows. Consider initial conditions on a line that contains a Cantor set of singularities. The Cantor set corresponds to particle trajectories that can enter the holes in the side planes of the tetrahedron and stay in the scattering region forever. Those that cannot enter the holes or enter the holes but escape in finite time correspond to gaps, also called intervals of continuity, between points in the Cantor set. Decreasing the size of the holes is equivalent to enlarging these gaps. For a binary self-similar Cantor set of primary gap size Δ, its box-counting dimension is

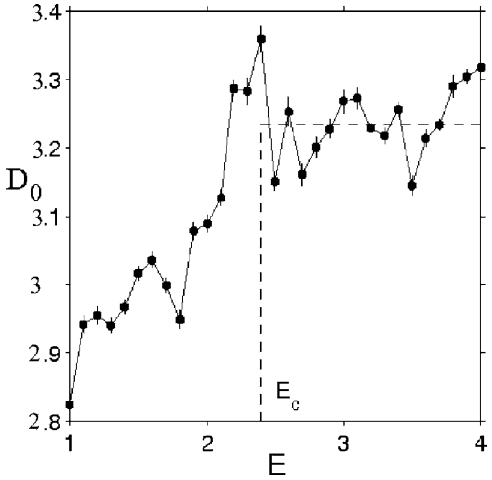

Fig. 8.15 Box-counting dimension D_0 of the chaotic saddle versus the energy E. The dimension remains practically constant for $E > E_c$ and decreases as E is decreased through $E_c \approx 2.25$ [444] (copyright 2000, the American Physical Society)

$$d_s = \frac{\ln 2}{\ln 2 - \ln(1-\Delta)}.$$

Assuming that $1-\Delta$ is proportional to s, the size of the holes, we obtain, using (8.58),

$$d_s \sim [A - B\ln(s_0 - C(E_c - E))]^{-1}, \tag{8.59}$$

for E slightly below E_c, where A and B are positive constants. This scaling relation indicates that the dimension of the chaotic saddle decreases as the energy E is decreased from the critical value E_c, due to the shrinkage of the holes in the side planes of the potential configuration.

Notice that for energies about $E < E_0 \approx E_c$, chaotic scattering does not occur if the system has only two degrees of freedom, due to the fact that the inaccessible regions are connected. Thus, for two-degree-of-freedom Hamiltonian systems (corresponding to two-dimensional area-preserving maps), no particle coming from outside the scattering region can enter the bounded, triangular-like region formed at the center of the potential hills. The dynamics in the bounded triangular-like region is typically made up of chaotic seas mixed with KAM tori. Although there is bounded chaos in this case, it is not accessible to particles from outside, and hence there is no chaotic scattering (Fig. 6.20a). In the case of three-degree-of-freedom systems (four-dimensional maps), in the same energy range, the corresponding classically allowed bounded region in the center of the potential hills is accessible to scattering particles coming from outside. Chaotic scattering is thus possible, which for this class of scattering systems is uniquely a high-dimensional phenomenon.

8.5.4 Topological Change Accompanying the Metamorphosis

The topology of chaotic scattering can be studied by examining the structure of *exit basins*. For the tetrahedron configuration, there are four side planes through which particles can exit. Suppose a large number of particles is launched toward the scattering region from a two-dimensional area in an (x-y)-plane at some large negative z position. After the scattering, the particles in the initial plane can be color-coded, depending on through which side plane they exit the system. Figure 8.16a shows, for $E = 4$, the basin structure in the area defined by $(-0.4 \leq x_0, y_0 \leq 0.4)$ in the

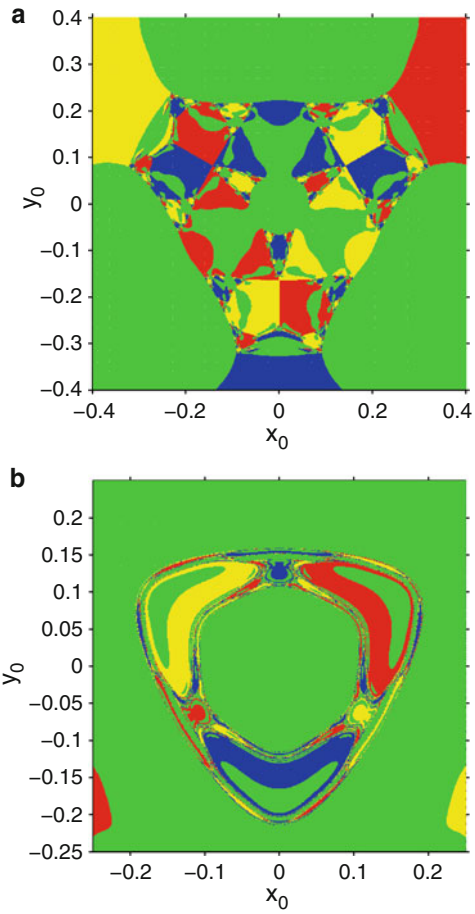

Fig. 8.16 Exit basins of scattering trajectories for (**a**) $E = 4$, and (**b**) $E = 1$. In (**a**), the basin boundaries common to the four colors consist of completely isolated points only. In (**b**), the part of the basin boundary common to the four colors is connected and it is Wada. See text for the meaning of the color coding [444] (copyright 2000, the American Physical Society)

plane located at $z_0 = -10.0$, where 500×500 particles uniformly distributed in the initial area are launched toward the scattering region along the $+z$-direction [444]. If a particle exits through the plane defined by vertices $(1,2,4)$ shown in Fig. 8.11 (or $(1,3,4)$, or $(1,2,3)$, or $(2,3,4)$), its location in the initial two-dimensional area is marked by red (or yellow, or blue, or green). As can be seen from Fig. 8.16a, the boundary contains isolated points where the four colors meet, but for almost all points on the boundary only two colors meet. The basin boundary is the set of intersecting points between the stable manifold of the chaotic saddle with the initial plane. For this energy, then, the common boundary points with different colors are isolated. As the energy is lowered, the previously classically forbidden regions become connected, and extended parts of the basin boundary points are now common to the four colors, as shown in Fig. 8.16b for $E = 1$. This is the Wada property of basins (Sect. 5.5). The topology of the basin undergoes a sudden change (metamorphosis) from being disconnected to being Wada at the critical energy value E_c.

For $E > E_c$, when the forbidden regions are disconnected (Fig. 8.12a), a scattering trajectory will typically enter the scattering region, bounce off the forbidden regions a number of times, and leave. As the particle leaves the scattering region, it crosses one of the side planes shown in Fig. 8.11. For typical trajectories, one can continuously change the initial conditions so as to cause a continuous change in the trajectory (this is not true if the initial condition lies on the stable manifold of the saddle, but such points have zero measure in the phase space). That is, there are paths in the space of initial conditions for which the escape parameters (such as escape angles, lifetime, etc.) change continuously, and these paths contain all initial conditions except for a set of measure zero. Now consider a subspace M in the full space of initial conditions, which can be chosen to have dimension two or higher. Consider one such path, denoted by C, that connects two points a and b in M belonging to two different escape basins, denoted by S_1 and S_2. Distinct side planes defining the different escapes are separated by segments that connect two adjacent triangular faces (Fig. 8.11). For $E > E_c$, parts of these segments lie outside the forbidden regions. Therefore, the path C in M can be chosen such that the corresponding trajectories go from one escape to a neighboring one continuously, without going through any other escape; in other words, all points in C belong to either S_1 or S_2. This corresponds to a basin boundary that separates only two escapes, and therefore to a non-Wada basin.

The picture described above completely changes when the energy goes below E_c. The forbidden regions are now connected into one single region, and the boundaries between the side planes that define the different escapes lie entirely within it. One can no longer go smoothly from one escape to another by a continuous change of initial conditions, due to the presence of forbidden regions separating the escape routes.

The change in the topological structure of the escape basin described above is possible only in three-dimensional physical space: it does not happen for two-degree-of-freedom systems, in which the basin boundaries in systems with three or more escapes typically have the Wada property (Sect. 5.5). The reason is that the forbidden regions separating distinct escapes can never be bypassed from one escape channel to another.

8.6 Superpersistent Transient Chaos: Basics

The type of transient chaos discussed so far, such as that induced by a boundary crisis, is characterized by the familiar algebraic scaling law (3.2) of its escape rate κ as a function of parameter variations in p. There exists, however, another distinct class of transient chaos: superpersistent transient chaos, characterized by the following scaling law:

$$\kappa \sim \exp\left[-C(p-p_c)^{-\chi}\right], \quad p > p_c, \tag{8.60}$$

where $C > 0$ and $\chi > 0$ are constants. As p approaches the critical value p_c from above, the transients become superpersistent in the sense that the exponent in the average transient lifetime

$$\tau \approx \frac{1}{\kappa} \sim \exp\left[C(p-p_c)^{-\chi}\right], \quad p > p_c,$$

diverges in an exponential-algebraic manner. This type of transient chaos is quite common in high-dimensional systems. Its origin can, however, be understood in simple models. For illustrative purposes we therefore shall again use here low-dimensional maps.

Superpersistent transient chaos was conceived to occur through the dynamical mechanism of unstable–unstable pair bifurcations. The same mechanism causes a riddling bifurcation that creates a riddled basin, so superpersistent chaotic transients can be expected at the onset of riddling [711]. It was shown that noise can also induce superpersistent chaotic transients under certain conditions. For a recent review, see [440].

8.6.1 Unstable–Unstable Pair Bifurcation

Unstable–unstable pair bifurcation represents a generic mechanism for superpersistent chaotic transients [294, 295, 455]. One can imagine two unstable periodic orbits of the same period, one on the chaotic attractor and another on the basin boundary, as shown in Fig. 8.17a. As a bifurcation parameter p reaches a critical value p_c, the

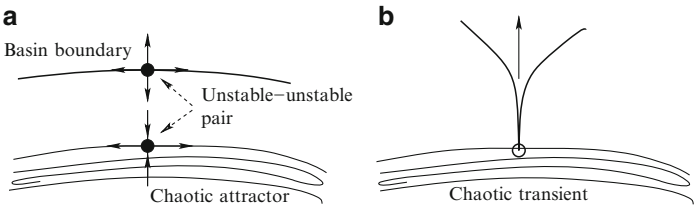

Fig. 8.17 Schematic illustration of an unstable–unstable pair bifurcation. (**a**) Invariant sets for $p < p_c$: a chaotic attractor, the basin boundary, and the pair of unstable periodic orbits. (**b**) For $p > p_c$, an escaping channel is created by an unstable–unstable pair bifurcation that converts the originally attracting motion into a chaotic transient

two orbits *coalesce* and disappear simultaneously, leaving behind a "channel" in the phase space through which trajectories on the chaotic attractor can escape, as shown in Fig. 8.17b. The chaotic attractor is thus converted into a nonattracting chaotic set, but the channel created by this mechanism is typically supernarrow [294, 295, 455]. Suppose that on average, it takes time $T(p)$ for a trajectory to travel through the channel in the phase space. We expect the tunneling time $T(p)$ to be infinite for $p = p_c$, but for $p > p_c$, the time becomes finite and decreases as p is increased from p_c. For p above but close to p_c, the tunneling time can be long.

From Fig. 8.17a, we see that if the phase space is two-dimensional, the periodic orbit on the attractor is a saddle and that on the basin boundary is a repeller. This can arise only if the map is noninvertible. Thus, the unstable–unstable pair bifurcation can occur in noninvertible maps of at least dimension two, or in invertible maps of at least dimension three (or in flows of dimension at least four).

Let $\lambda_1 > 0$ be the largest average Lyapunov exponent of the chaotic attractor. After an unstable–unstable pair bifurcation the opened channel is locally transverse to the attractor. A trajectory that spends time $T(p)$ in the channel opened up at an unstable periodic orbit on the attractor, the *mediating orbit* involved in the unstable–unstable pair bifurcation, must come to within distance of about $\exp[-\lambda_1 T(p)]$ from this orbit. The probability for this to occur is proportional to $\exp[-\lambda_1 T(p)]$. The average time for the trajectory to remain on the earlier attractor, or the average transient lifetime, can be related to the tunneling time as

$$\tau(p) \sim \exp[\lambda_1 T(p)],$$

or equivalently,

$$\kappa(p) \sim \exp[-\lambda_1 T(p)]. \tag{8.61}$$

The tunneling time thus determines the scaling of the escape rate with the parameter variation.

Since the escaping channel is extremely narrow, the dynamics in the channel is approximately one-dimensional along the direction from the mediating periodic orbit to the orbit on the basin boundary, as schematically shown in Fig. 8.17. The basic dynamics can be captured through the following simple one-dimensional map:

$$x_{n+1} = x_n^{k-1} + x_n + p, \tag{8.62}$$

where x denotes the dynamical variable in the channel, $k \geq 3$ is an odd integer to generate two real fixed points, and p is a bifurcation parameter with critical point $p_c = 0$. For $p < p_c = 0$, the map has a stable fixed point $x_s = -|p|^{1/(k-1)}$ and an unstable fixed point $x_u = |p|^{1/(k-1)}$, which collide at p_c and disappear for $p > p_c$, mimicking an unstable–unstable pair bifurcation. Since for $0 < p \ll 1$, $T(p)$ is large (see Sect. 2.4), the map (8.62) can be approximated by the following differential equation:

$$\frac{dx}{dt} = x^{k-1} + p. \tag{8.63}$$

Suppose the root of the channel is $x = 0$ and its length is l. The tunneling time is then

$$T(p) \approx \int_0^l \frac{\mathrm{d}x}{x^{k-1} + p} \sim p^{-\frac{k-2}{k-1}}. \tag{8.64}$$

Substituting (8.64) into (8.61) gives

$$\kappa(p) \sim \exp\left(-Cp^{-\frac{k-2}{k-1}}\right), \tag{8.65}$$

where $C > 0$ is a constant. We see that as p approaches the critical value $p_c = 0$ from above, the average transient lifetime diverges in an exponential-algebraic way, giving rise to superpersistent transients. The exponent χ in the scaling law (8.60) thus assumes the value $(k-2)/(k-1) < 1$.

To give a concrete example, we use the class of noninvertible two-dimensional maps considered by Grebogi, Ott, and Yorke [294, 295]:

$$\theta_{n+1} = 2\theta_n \bmod 2\pi, \quad z_{n+1} = az_n + z_n^2 + \beta\cos\theta_n, \tag{8.66}$$

where a and β are parameters. Because of the z_n^2 term in the z-equation, for large z_n we have $|z_{n+1}| > |z_n|$. There is thus an attractor at $z = +\infty$. Near $z = 0$, depending on the choice of the parameters, there can be either a chaotic attractor or none. For instance, for $0 < \beta \ll 1$, there is a chaotic attractor near $z = 0$ for $a < a_c = 1 - 2\sqrt{\beta}$, and the attractor becomes a chaotic repeller for $a > a_c$ [294]. The chaotic attractor, its basin of attraction, and part of the basin of the infinity attractor are shown in Fig. 8.18.

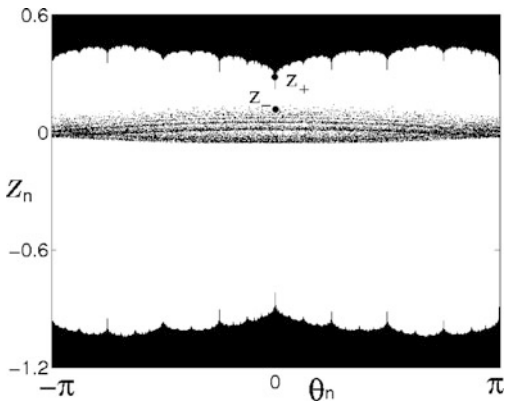

Fig. 8.18 Phase space of the two-dimensional map model (8.66): a chaotic attractor near $z = 0$ (*black*), its basin of attraction (*blank*), and the basin of the attraction of the attractor at $z = +\infty$ (*black*) for $a = 0.5$ and $\beta = 0.04$, before the unstable–unstable pair bifurcation ($a_c = 0.6$). The fixed points $z_\pm$ are marked [294] (copyright 1983, the American Physical Society)

Following the argument leading to the scaling law (8.65), one can see that the map (8.66) allows for superpersistent transients for $a > a_c$. In particular, for $a < a_c$ there are two fixed points: $(0, z_+)$ and $(0, z_-)$, where $z_\pm = \left(1 - a \pm \sqrt{(1-a)^2 - 4\beta}\right)/2$, on the basin boundary and on the chaotic attractor, respectively. They coalesce at $a = a_c$. For $a > a_c$, a channel is created through which trajectories on the original attractor can escape to the attractor at infinity. At the location of the channel where $\theta = 0$, the z-mapping becomes

$$z_{n+1} = az_n + z_n^2 + \beta.$$

Letting $\delta = z - z_*$, where $z_* = (1-a)/2$, we obtain

$$\delta_{n+1} = \delta_n^2 + \delta_n + b, \tag{8.67}$$

with $b = \sqrt{\beta}(a - a_c) - [(a - a_c)/2]^2$. For $a \approx a_c$, we have $b \approx \sqrt{\beta}(a - a_c)$. Equation (8.67) is identical to (8.62) with $k = 3$. The integral (8.64) then yields $T \approx \pi b^{-1/2}/2$. The Lyapunov exponent is determined by the θ-dynamics: $\lambda_1 = \ln 2$. Using (8.61), we obtain the scaling of the escape rate for $a > a_c$ as

$$\kappa(a) \sim \mathrm{e}^{-T \ln 2} \approx \mathrm{e}^{(-\pi \ln 2/2) b^{-1/2}} \approx \mathrm{e}^{-C(a - a_c)^{-1/2}}, \tag{8.68}$$

where $C = \pi(\ln 2)\beta^{-1/4}/2$ is a positive constant.

8.6.2 *Riddling Bifurcation and Superpersistent Chaotic Transients*

In Sect. 5.7, the phenomenon of riddling, or riddled basins in dynamical systems with symmetry, is described. The presence of symmetry often leads to an invariant subspace. In the absence of symmetry-breaking or random perturbations, a trajectory originated in the invariant subspace remains there forever. Situations can also be expected whereby a chaotic attractor lies in the invariant subspace. As discussed, one such example is the system of coupled, identical chaotic oscillators. The synchronization manifold is naturally a low-dimensional invariant subspace in the full phase space that can be high-dimensional if the number of oscillators is large. If another attractor exists outside the invariant subspace, riddling can occur in the sense that the basin of the chaotic attractor in the invariant subspace is riddled with holes of all sizes that belong to the basin of the other attractor. Imagine the situation in which all unstable periodic orbits embedded in the chaotic attractor are stable with respect to perturbations in the direction transverse to the invariant subspace. In this case, almost all initial conditions in the vicinity of the invariant subspace lead to trajectories that end up asymptotically on the chaotic attractor. Riddling bifurcation refers to the situation in which when a system parameter changes, an unstable periodic orbit

(usually of low period) embedded in the chaotic attractor becomes transversely unstable. An immediate physical consequence of the riddling bifurcation is that when there is a small amount of symmetry-breaking, an extraordinarily low fraction of the trajectories in the invariant subspace diverge, as shown in Fig. 5.21.

Due to nonlinearity, a "tongue" opens at $\mathbf{x}_{\rm p}$, allowing trajectories near the invariant subspace to escape for $p > p_{\rm c}$, as shown in Fig. 5.20b. Each preimage of $\mathbf{x}_{\rm p}$ also develops a tongue simultaneously. Since preimages of $\mathbf{x}_{\rm p}$ are dense in the invariant subspace, an infinite number of tongues open up simultaneously at $p = p_{\rm c}$, indicating that initial conditions arbitrarily close to the invariant subspace can approach another attractor. Trajectories in the chaotic attractor remain there even for $p > p_{\rm c}$, since the subspace in which the chaotic attractor lies is invariant and each tongue has zero width there. But trajectories near the chaotic attractor have a finite probability of being in the open and dense set of tongues. Trajectories having initial conditions in the tongues approach asymptotically the other attractor. The basin of attraction of the chaotic attractor is thus a Cantor set of leaves of positive Lebesgue measure (a fat fractal), signifying riddling. Physically, since the onset of riddling induces the creation of these supernarrow tongues near the invariant subspace, it leads to superpersistent chaotic transient behavior in the vicinity of the chaotic attractor. For points chosen at random at a small distance d from the attractor, the probability of not being attracted depends on the distance d as

$$P(d) \sim \exp[-Kd^{-\gamma}], \tag{8.69}$$

where $\gamma > 0$ is a positive exponent, and $K > 0$ is a constant. In the presence of symmetry-breaking as characterized by the parameter ε, a similar argument leads to the escape rate

$$\kappa(\varepsilon) \sim \exp[-K\varepsilon^{-\gamma}], \tag{8.70}$$

for initial conditions in the original invariant subspace.

To make these ideas more concrete, it is convenient to use the following extension of the noninvertible two-dimensional map (5.24) [455]:

$$\begin{aligned} x_{n+1} &= rx_n(1-x_n), \\ y_{n+1} &= \varepsilon + p\mathrm{e}^{-b(x_n-x_{\rm p})^2}y_n + y_n^3, \end{aligned} \tag{8.71}$$

where for $\varepsilon = 0$, $y = 0$ defines the invariant subspace, $r,\ b > 0$ are parameters, and p is the bifurcation parameter. The broken symmetry is with respect to $y \to -y$. The dynamics in the invariant subspace is described by the logistic map $x_{n+1} = rx_n(1-x_n)$, for which chaotic attractors can arise.

In the symmetric case ($\varepsilon = 0$), the two eigenvalues of the unstable fixed point $\mathbf{x}_{\rm p}$ ($x_{\rm p} = 1 - 1/r, y = 0$) are $(2-r, p)$. Thus, $\mathbf{x}_{\rm p}$ is stable in the y direction for $p < 1$ and unstable for $p > 1$. This fixed point is a saddle for $r > 3$ and $p < 1$. For $p < 1$, there are two other unstable fixed points located at $\mathbf{r}_{\pm} \equiv (x_{\rm p}, \pm\sqrt{1-p})$. These two fixed points have eigenvalues $(2-r, 3-2p)$, both pure repellers for $r > 3$ and $p < 1$, as

shown in Fig. 5.20a. The two repellers collide with each other and with the saddle at $p = p_c = 1$ in a saddle-repeller bifurcation. They do not exist for $p > 1$. Thus, for $p > 1$, two tongues, symmetrically located with respect to the invariant subspace, open up at $x = x_p$, allowing trajectories near $y = 0$ to escape to $|y| = \infty$, since the cubic term in the $y-$dynamics guarantees that if $|y_n| > 1$, then $|y_{n+1}| > |y_n| > 1$. Once a trajectory reaches $|y| = 1$, its y value approaches infinity rapidly. So $|y| = \infty$ can be regarded as the second attractor of (8.71) besides the chaotic attractor in the $y = 0$ plane (invariant subspace), which exists for $r > 3.6$.

When there is symmetry-breaking ($\varepsilon > 0$), trajectories can leave the original chaotic attractor at $y = 0$ ($y = 0$ is no longer an invariant subspace), and hence the attractor is converted into a chaotic saddle. Simulation of (8.71) showed that only an exceedingly small fraction of the points at $y = 0$ diverges toward the $|y| = \infty$ attractor. The transient time can easily be longer than, say, 10^5 iterations even for $\varepsilon = 0.014$. To obtain the scaling of the escape rate with the symmetry-breaking parameter, the first step is to estimate, for $\varepsilon \geq 0$, the size δ of the tongue at $y = 0$ for a trajectory of transient time $T(\varepsilon)$. Since the $y = 0$ attractor is chaotic, its maximum Lyapunov exponent λ_1 is positive. Let $L_u = e^{\lambda_1} > 1$, which is the stretching factor for an infinitesimal vector in the x direction. That the transient time, the time needed to reach a distance of order unity, is T implies $\delta L_u^T \approx 1$, which gives

$$\delta \approx {L_u}^{-T}. \tag{8.72}$$

The next step is to examine the probability that a trajectory falls into the tongue of size δ at $y = 0$ for $\varepsilon \geq 0$, which is proportional to δ. The average time for a trajectory to fall into the tongue is

$$\tau \sim \delta^{-1} \approx {L_u}^T = \exp(\lambda_1 T). \tag{8.73}$$

The final step is to evaluate T, the time it takes for the trajectory to exit once it has fallen into the tongue. Near x_p, we have $\exp[-b(x_n - x_p)^2] \approx 1$. For initial conditions chosen at $y_0 = 0$, the trajectory satisfies $y_n \geq \varepsilon$ for $n \geq 1$. For small ε it takes many iterations for a trajectory to reach $y = 1$. Thus, the y-dynamics within the tongue can be approximated by the differential equation

$$\frac{dy}{dt} = \varepsilon + y^3.$$

This gives

$$T = \int_0^1 \frac{dy}{\varepsilon + y^3} = \varepsilon^{-2/3} \int_0^{\varepsilon^{-1/3}} \frac{dz}{1 + z^3}. \tag{8.74}$$

For $\varepsilon \to 0$ the integral converges to $C = \pi/3^{3/2}$. Substitution of this expression into (8.73) and using $\kappa \approx 1/\tau$ yields the following scaling of the escape rate:

$$\kappa \sim \exp[-C\lambda_1 \varepsilon^{-2/3}], \tag{8.75}$$

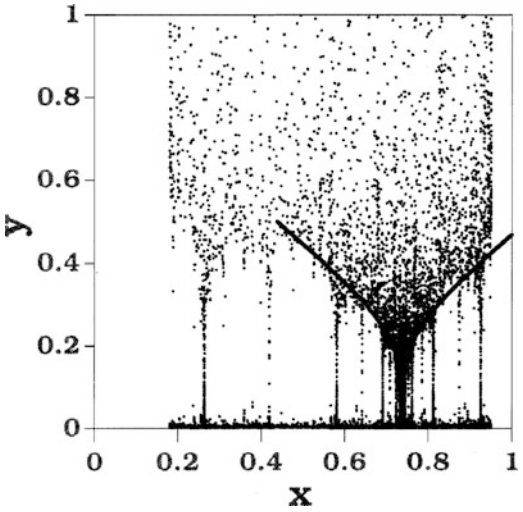

Fig. 8.19 Mushroom-shaped phase-space regions (tongues) through which trajectories escape the $y = 0$ chaotic attractor ($r = 3.8$) at $p = 1.18 > p_c = 1$ and $\varepsilon = 0.005$ in (8.71) [455] (copyright 1996, the American Physical Society)

which is the scaling law (8.70) with $K \equiv C\lambda_1$. In (8.75), the exponent $2/3$ is a consequence of the y^3 term in the y-dynamics. If this term is replaced by, say, a y^2 term, the exponent will be $1/2$. Thus, the exponent $2/3$ in (8.75) is specific to the two-dimensional map model (8.71). However, the scaling relation (8.70) is general, with the exponent γ being positive.

The escaping behavior of trajectories, once they have fallen into the tongue, can be seen by monitoring their traces in the phase space before they reach $y = 1$. Since the tongues are supernarrow at $p = p_c$, it is numerically convenient to examine the case of $p > p_c$, but for p close to p_c. Figure 8.19 shows the last 50 points of 600 trajectories before they reach $y = 1$. There is a "mushroom-shaped" (tongue) crowd of trajectory points in the phase space located above the fixed point $x_p \approx 0.7368$. The solid curves in Fig. 8.19 indicate the envelope of the tongue, which can be derived analytically by considering the escaping dynamics in the vicinity of x_p. Specifically, after a trajectory falls into the escaping channel located at x_p, its dynamics can be approximated by

$$(x_{n+1} - x_p) \approx (2 - r)(x_n - x_p), \quad y_{n+1} \approx \varepsilon + py_n + y_n^3.$$

By introducing $z_n \equiv |x_n - x_p|$, the x-dynamics becomes $z_{n+1} = |2 - r|z_n = (r - 2)z_n$. For p close to p_c and ε small, it takes an extremely large number of iterations for a typical trajectory to escape due to the long chaotic transient. We thus have

$$dz/dt = (r - 3)z, \quad dy/dt = \varepsilon + (p - 1)y + y^3. \tag{8.76}$$

This implies that for $\varepsilon \approx 0$, we have $\mathrm{d}z/\mathrm{d}y = (r-3)z/[(p-1)y+y^3]$, which leads to

$$z(y) = \left(\frac{y}{\sqrt{(p-1)+y^2}} \right)^{(r-3)/(p-1)}, \quad \text{for } p > p_c = 1. \tag{8.77}$$

The solid curves in Fig. 8.19 are $[x_p \pm z(y)]$, respectively. They represent the envelope of the tongue reasonably well.

8.7 Superpersistent Transient Chaos: Effect of Noise and Applications

8.7.1 Noise-Induced Superpersistent Chaotic Transients

In the general setting, in which an unstable–unstable pair bifurcation can occur, noise can induce superpersistent transients *preceding* the bifurcation. Consider, in the noiseless case, a chaotic attractor in its basin of attraction ($p < p_c$). When noise is present, there can be a nonzero probability that two periodic orbits, one belonging to the attractor and the other to the basin boundary, can get close and coalesce *temporally*, giving rise to a nonzero probability that a trajectory on the chaotic attractor crosses the basin boundary and moves toward the basin of another attractor. Transient chaos thus arises even for $p < p_c$. Due to weak noise, the channels through which trajectory escapes the chaotic attractor open and close intermittently in time. Escaping through the channel requires the trajectory to stay in a small vicinity of the opening of the channel for a finite amount of time, which occurs with extremely small probability. The creation of the channel by noise and the noisy dynamics in the channel are thus the key ingredients to the noise-induced transient behavior.

For a two-dimensional phase space, the situation described above is schematically illustrated in Fig. 8.17a, b for the cases in which noise is respectively absent and present. If the attractor is close to the basin boundary, noise of strength σ can induce an unstable–unstable pair bifurcation, creating a narrow channel through which trajectories can escape, as shown in Fig. 8.17b even for $p < p_c$. As (8.61) suggests, the escape rate can be expressed in terms of the tunneling time $T(p,\sigma)$ as

$$\kappa(p,\sigma) \sim \exp[-\lambda_1 T(p,\sigma)], \tag{8.78}$$

where $\lambda_1 > 0$ is the largest Lyapunov exponent of the original chaotic attractor. Again, since the escaping channel is extremely narrow, for $T(p,\sigma)$ large, the dynamics is approximately one-dimensional in the channel along which the periodic orbit on the attractor is stable but the orbit on the basin boundary is unstable for $p < p_c$ (Fig. 8.17a). This feature can thus be captured through the stochastic version of the map (8.62):

$$x_{n+1} = x_n^{k-1} + x_n + p + \sigma\xi_n, \tag{8.79}$$

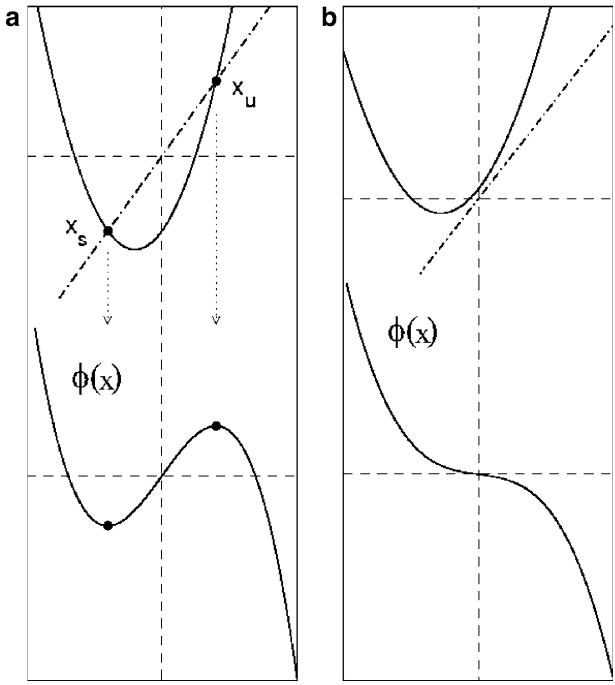

Fig. 8.20 Dynamics of the map (8.79), for $k = 3$ (**a**) in the subcritical cases ($p < 0$), and (**b**) in the supercritical case ($p > 0$). *Upper graph*: deterministic map ($\sigma = 0$), *lower graph*: quasipotential $\Phi(x)$

where $\sigma \ll 1$ is the noise amplitude and ξ_n is a Gaussian random variable of zero mean and unit variance. For $T \gg 1$, (8.79) can be approximated by the Langevin equation

$$\frac{\mathrm{d}x}{\mathrm{d}t} = x^{k-1} + p + \sigma\xi(t) \equiv -\frac{1}{2}\frac{\mathrm{d}\Phi}{\mathrm{d}x} + p + \sigma\xi(t), \tag{8.80}$$

where the function

$$\Phi(x) = -2(x^k/k + px) \tag{8.81}$$

is the associated quasipotential of the one-dimensional problem (see Sect. 4.2). For $p < 0$, the underlying deterministic system for (8.80) has a stable fixed point $x_\mathrm{s} = -|p|^{1/(k-1)}$ and an unstable fixed point $x_\mathrm{u} = |p|^{1/(k-1)}$. For $p > 0$, there are no fixed points, as shown in Fig. 8.20. It is convenient to define the opening x_r of the channel at the stable fixed point $x_\mathrm{r} = x_\mathrm{s}$ when it exists, i.e., for $p < 0$, and set $x_\mathrm{r} = 0$ otherwise. A properly formulated first-passage-time problem for this one-dimensional stochastic process can yield the scaling of $T(p, \sigma)$ [198, 199] as follows.

Let $P(x,t)$ be the probability density function of the stochastic process described by (8.80) that satisfies the Fokker–Planck equation:

$$\frac{\partial P(x,t)}{\partial t} = -\frac{\partial}{\partial x}[(x^{k-1}+p)P(x,t)] + \frac{\sigma^2}{2}\frac{\partial^2 P}{\partial x^2}. \tag{8.82}$$

Let l be the effective length of the channel in the sense that a trajectory with $x > l$ is considered to have escaped the channel. The tunneling time $T(p,\sigma)$ required for a trajectory to travel through the channel is equivalent to the mean first passage time from the opening $x_{\rm r}$ of the channel to l. For an escaping trajectory, once it falls into the channel through $x_{\rm r}$, it will eventually exit the channel at $x = l$ without even going back to the original chaotic attractor. This is so because the probability for a trajectory to fall into the channel and then to escape is already exponentially small, (8.78), and hence the probability for any "second-order" process to occur, whereby a trajectory falls into the channel, moves back to the original attractor, and falls back in the channel again, is negligible. For trajectories in the channel there is thus a reflecting boundary condition at $x = x_{\rm r}$,

$$\left[(x^{k-1}+p)P(x,t) - \frac{\sigma^2}{2}\frac{\partial P}{\partial x}\right]\Bigg|_{x=x_{\rm r}} = 0, \tag{8.83}$$

and an absorbing boundary condition at $x = l$,

$$P(l,t) = 0. \tag{8.84}$$

Assuming that trajectories initially are near the opening of the channel (but in the channel), we have the initial condition

$$P(x,x_{\rm r}) = \delta(x - x_{\rm r}^{+}). \tag{8.85}$$

Under these boundary and initial conditions, the solution to the Fokker–Planck equation yields the following mean first-passage-time [256, 640] for the stochastic process (8.80):

$$T(p,\sigma) = \frac{2}{\sigma^2}\int_{x_{\rm r}}^{l} {\rm d}y \exp\left[\frac{\Phi(y)}{\sigma^2}\right]\int_{x_{\rm r}}^{y}\exp\left[\frac{-\Phi(y')}{\sigma^2}\right]{\rm d}y'. \tag{8.86}$$

The double integral in (8.86) can be carried out [198, 199] for the three distinct cases critical ($p = 0$), supercritical ($p > 0$), and subcritical ($p < 0$).

In the weak-noise regime ($\sigma \ll \sigma_{\rm c} \sim |p|^{k/(2(k-1))}$), the results can be summarized as

$$T(p,\sigma) \sim \begin{cases} p^{-(k-2)/(k-1)}, & p > 0, \\ \sigma^{-(2-4/k)}, & p = 0, \\ |p|^{-(k-2)/(k-1)}\exp\left(|p|^{k/(k-1)}/\sigma^2\right), & p < 0. \end{cases} \tag{8.87}$$

These laws imply the following scaling laws for the escape rate of the chaotic transients in various regimes (substituting the expressions of $T(p,\sigma)$ in (8.78)):

$$\kappa(p,\sigma) \sim \begin{cases} \exp\left[-Cp^{-(k-2)/(k-1)}\right], & p > 0, \\ \exp\left[-C\sigma^{-(2-4/k)}\right], & p = 0, \\ \exp\left(-C|p|^{-(k-2)/(k-1)} \exp[|p|^{k/(k-1)}/\sigma^2]\right), & p < 0. \end{cases} \tag{8.88}$$

The general observation is that different behaviors arise depending on the bifurcation parameter p: independent of noise for the supercritical regime, normally superpersistent for the critical case, and extraordinarily superpersistent for the subcritical regime in the sense of scaling in (8.88) (for $p < 0$). Numerical support for these distinct scaling behaviors was obtained [198, 199].

8.7.2 *Application: Advection of Inertial Particles in Open Chaotic Flows*

We will see in Chap. 10 that the inertia of the advective particles alters the advective dynamics, and the underlying dynamical system becomes dissipative so that attractors can arise, and hence particles can be trapped permanently in some region in the physical space. The possibility that toxin particles can be trapped in physical space is particularly worrisome. It is thus interesting to study the structural stability of such attractors. In particular, can chaotic attractors so formed be persistent under small noise? It was found [197] that in general, the attractor is destroyed by weak noise and replaced by a chaotic transient, which is typically superpersistent. For weak noise, the extraordinarily long trapping time makes the transient particle motion practically equivalent to an attracting motion with similar physical or biological effects.

Noise in the context of particle advection can be due, for example, to the diffusivity of the advected particles [143]. Diffusion can be generated by, e.g., microscopic interactions (molecular diffusion). The dimensionless equation of motion of an inertial particle will be detailed in Chap. 10. The noisy version of this equation in a two-dimensional incompressible flow $\mathbf{u}(x,y,t)$ in the horizontal plane is

$$\ddot{\mathbf{r}}(t) = A\left[\mathbf{u}(\mathbf{r}(t),t) - \dot{\mathbf{r}}(t)\right] + \frac{3}{2}R\frac{\mathrm{d}}{\mathrm{d}t}\mathbf{u}(\mathbf{r}(t),t) + \sigma\boldsymbol{\xi}(t), \tag{8.89}$$

where $\boldsymbol{\xi}(t) = (\xi_x(t), \xi_y(t))$, and $\xi_x(t)$ and $\xi_y(t)$ are independent Gaussian random variables of zero mean and unit variance, and σ is the noise amplitude. Parameters A and R are the inertial parameter and the density ratio, respectively, as defined in (10.29). The noise-free dynamics in a given time-periodic flow, the so-called

von Kármán vortex street around a cylinder, will be described in Sect. 10.7. There are three attractors [53]: two chaotic ones about the cylinder and a regular one at $x = \infty$. We present here the main effect due to noise because of its close relation to superpersistent chaotic transients.

Because of the explicit time dependence in the flow velocities, the attractors and their basins move oscillatorily around the cylinder. The remarkable feature is that in the physical space, there are time intervals during which the attractors come close to the basin boundaries. Thus, under noise, we expect permanently trapped motion on any one of the two chaotic attractors to become impossible. In particular, particles can be trapped near the cylinder, switching intermittently on the two originally chaotic attractors, but this can last only for a finite amount of time: eventually all trajectories on these attractors escape and approach the $x = \infty$ attractor. That is, chaos becomes transient if one takes into account the effect of noise, or equivalently, of diffusivity.

To understand the nature of this noise-induced transient chaos, one can distribute a large number of particles in the original basins of the chaotic attractors and examine the channel(s) through which they escape to the $x = \infty$ attractor under noise. Figure 8.21a–c show, for three dimensionless instants of time (1, $1/4$, and $1/2$ mod

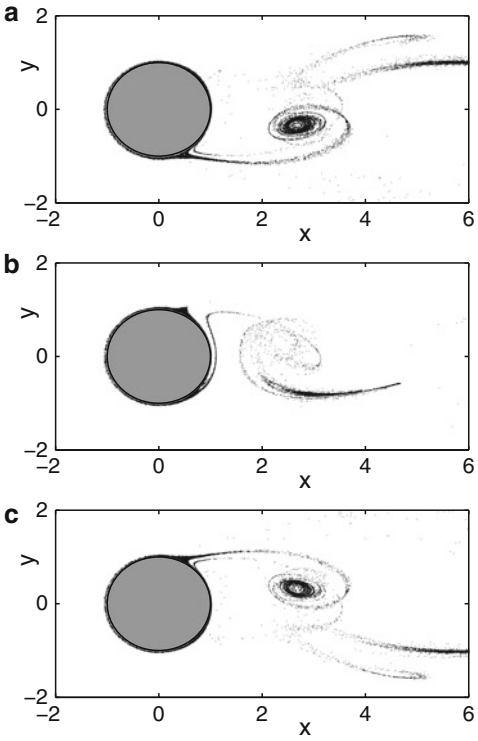

Fig. 8.21 (**a**)–(**c**) At three different instants of time, $1/4$ time units apart, locations of the temporally trapped and escaping inertial particles in the von Kármán vortex street in the presence of noise [197] (copyright 2000, the American Physical Society)

(1), respectively), locations of an ensemble of particles in the physical space. While there are particles still trapped in the original attractors, many others are already away from the cylinder. Since this is a two-dimensional projection of the full particle dynamics, some fractal-like features overlap. The escaping channels through which particles escape form a set of thin openings surrounding the cylinder and extending to one of the von Kármán vortices in the flow. After wandering near the vortex, particles go to the $x = \infty$ attractor. In the physical space the locations of these openings vary in time, but the feature that they are narrow is common.

For a fixed noise amplitude, the lifetimes of the particles near the cylinder obey an extremely slow decaying distribution. A least-squares fit gives [197] the escape rate as a function of the noise amplitude σ as

$$\kappa \approx \frac{1}{\tau} \approx \exp(-3.3\sigma^{-0.55}). \tag{8.90}$$

Note that for $\sigma = 0$, there is an attracting motion, so that κ vanishes. The way that κ goes to zero follows the superpersistent transient scaling law as σ is decreased.

Theoretically, the observed noise-induced superpersistent chaotic transient behavior can be explained using the approach in Sect. 8.7.1. The result implies that it may be possible to observe superpersistent chaotic transients in physical space. The flow system used for experimental study of advective chaotic scattering by Sommerer and coworkers (Fig. 8.19) is a possible candidate.